Document downloaded from:

http://hdl.handle.net/10251/196905

This paper must be cited as:

Gallego-Parra, S.; Gomis, O.; Vilaplana Cerda, RI.; Cuenca-Gotor, VP.; Martínez-García, D.; Rodríguez-Hernández, P.; Muñoz, A.... (2021). Pressure-induced order-disorder transitions in beta-In2S3: an experimental and theoretical study of structural and vibrational properties. Physical Chemistry Chemical Physics. 23(41):23625-23642. https://doi.org/10.1039/d1cp02969j

The final publication is available at

https://doi.org/10.1039/d1cp02969j

Copyright The Royal Society of Chemistry

Additional Information

ARTICLE

Pressure-induced order-disorder transitions in β-In_2S_3: an experimental and theoretical study of structural and vibrational properties

Samuel Gallego-Parra,[a*] Óscar Gomis,[b*] Rosario Vilaplana,[b] Vanesa Paula Cuenca-Gotor,[a] Domingo Martínez-García,[c] Plácida Rodríguez-Hernández,[d] Alfonso Muñoz,[d] Aldo Romero,[e] Arnab Majumdar,[f,g] Rajeev Ahuja,[f,h] Catalin Popescu[i] and Francisco Javier Manjón[a]

This joint experimental and theoretical study of the structural and vibrational properties of β-In_2S_3 upon compression shows that this tetragonal defect spinel undergoes two reversible pressure-induced order-disorder transitions up to 20 GPa. We propose that the first high-pressure phase above 5.0 GPa has the cubic defect spinel structure of α-In_2S_3 and the second high-pressure phase (ϕ-In_2S_3) above 10.5 GPa has a defect α-$NaFeO_2$-type (*R*-3*m*) structure. This phase, related to the NaCl structure, has not previously observed in spinels under compression and is related to both the tetradymite structure of topological insulators and to the defect $LiTiO_2$ phase observed at high pressure in other thiospinels. Structural characterization of the three phases shows that α-In_2S_3 is softer than β-In_2S_3 while ϕ-In_2S_3 is harder than β-In_2S_3. Vibrational characterization of the three phases is also provided, and their Raman-active modes tentatively assigned. Our work shows that the metastable α phase of In_2S_3 can be accessed not only by high temperature or varying composition but also by high pressure. On top of that, the pressure-induced β-α-ϕ sequence of phase transitions evidences that β-In_2S_3, a $B^{III}{}_2X^{V}{}_3$ compound with an intriguing structure typical of $A^{II}B^{III}{}_2X^{VI}{}_4$ compounds (intermediate between thiospinels and ordered-vacancy compounds) undergoes: i) a first phase transition at ambient pressure to a disordered spinel-type structure (α-In_2S_3), isostructural with those found at high pressure and high temperature treatment in other $B^{III}{}_2X^{V}{}_3$ compounds; and ii) a second phase transition to the defect α-$NaFeO_2$-type structure (ϕ-In_2S_3), a distorted NaCl-type structure that is related to the defect NaCl phase found at high pressure in $A^{II}B^{III}{}_2X^{VI}{}_4$ ordered-vacancy compounds and to the defect $LiTiO_2$-type phase found at high pressure in $A^{II}B^{III}{}_2X^{VI}{}_4$ thiospinels. This result shows that In_2S_3 (with its intrinsic vacancies) has a similar pressure behaviour than thiospinels and ordered-vacancy compounds of the $A^{II}B^{III}{}_2X^{VI}{}_4$ family, making β-In_2S_3 the union link between such families of compounds and showing that group-13 thiospinels have more in common to ordered-vacancy compounds than to oxospinels and thiospinels with transition metals.

Introduction

Spinels constitute a class of technologically important materials used in a wide range of applications, such as in dielectrics, sensors, solar cells, and energy materials. High-performance In-based nontoxic (Cd free) semiconductors are under the attentive watch of the industry to implement reliable and eco-friendly devices due to the environmental and biological issues concerning the use of toxic semiconductors in an ever-increasing demand for solar cells. In this context, In-based semiconductors, like spinel-type In_2S_3, have drawn a relevant interest for buffer layers to replace CdS. More specifically, several works have evaluated In_2S_3-buffered thin films in solar cells, achieving efficiencies between 12.9 and 16.4% by various deposition techniques.[1-3] These results make In_2S_3 a worthy competitor of CdS in solar cells. Moreover, as an n-type semiconductor, In_2S_3 exhibits a bandgap around 2.2 eV (depending on the growth conditions),[4-6] a high optical transmission in the visible region,[7] modest electrical transport properties,[8] a low lattice thermal conductivity[9], and excellent chemical stability.

Due to the above properties, different In_2S_3 phases have been exploited not only in buffer layers, but also in other devices and applications, such as photodetectors, lithium-ion batteries, oxygen sensors, as well as in thermoelectric, luminescent, and photocatalytic applications.[10-16] Up to three phases of In_2S_3 have been described at ambient pressure and different temperatures: i) the β phase, with tetragonal defect spinel structure (space group (S.G.) $I4_1/amd$, Z=16, **Fig. 1a)**) at ambient temperature; ii) the α phase, with cubic defect spinel structure (S.G. *Fd*-3*m*, Z=10.67, **Fig. 1b)**) above 749 K; and iii) the γ phase, with trigonal structure (S.G. *P*-3*m*1, Z=1) above 1100 K.

[a.] *Instituto de Diseño para la Fabricación y Producción Automatizada, MALTA Consolider Team, Universitat Politècnica de València, 46022 València, Spain*
[b.] *Centro de Tecnologías Físicas, MALTA Consolider Team, Universitat Politècnica de València, 46022 València, Spain*
[c.] *Departamento de Física Aplicada-ICMUV-MALTA Consolider Team, Universitat de València, c/Dr. Moliner 50, 46100 Burjassot (València), Spain*
[d.] *Departamento de Física, Instituto de Materiales y Nanotecnología, MALTA Consolider Team, Universidad de La Laguna, 38207 San Cristóbal de La Laguna, Spain*
[e.] *Physics Department, West Virginia University, Morgantown, 26505, USA*
[f.] *Department of Physics and Astronomy, Box 516, Uppsala University, Uppsala, SE-75120, Sweden*
[g.] *Département de Physique and Regroupement Québécois sur les Matériaux de Pointe, Université de Montréal, C. P. 6128, Succursale Centre-Ville, Montréal, Québec H3C 3J7, Canada*
[h.] *Department of Physics, Indian Institute of Technology Ropar, Rupnagar 140001, Punjab, India*
[i.] *ALBA-CELLS, MALTA Consolider Team, 08290 Cerdanyola del Valles (Barcelona), Catalonia, Spain*

† *Electronic Supplementary Information (ESI) available: [details of any supplementary information available should be included here]. See DOI: 10.1039/x0xx00000x*

Please do not adjust margins

The stable phase at ambient conditions, β-In_2S_3, features In cations occupying 2/3 of tetrahedral (Td) positions, the Td(8e) sites, and totally occupying octahedral positions (Oh), the Oh(16h), and Oh(8c) sites. Curiously, 1/3 of the Td positions, the Td(4a) sites, are empty.[17-21] No other $B^{III}{}_2X^{VI}{}_3$ compound shows the defect spinel structure at ambient pressure to our knowledge and only Al_2S_3 and Al_2Se_3 are known to show this phase at high pressure (HP) and high temperature (HT).[22, 23] Indeed, the empty Td(4a) sites can be treated as ordered vacancies, so β-In_2S_3 is in fact the only In-based ordered-vacancy compound (OVC). In this context, β-In_2S_3 can be considered a defective $A^{II}B^{III}{}_2X^{VI}{}_4$ compound (it can be reformulated as $In_{0.66}In_2S_4$ and found at the ICSD database). This material is located between $A^{II}B^{III}{}_2X^{VI}{}_4$ compounds with cubic spinel structure and those with defect chalcopyrite and defect stannite (or famatinite) structures.

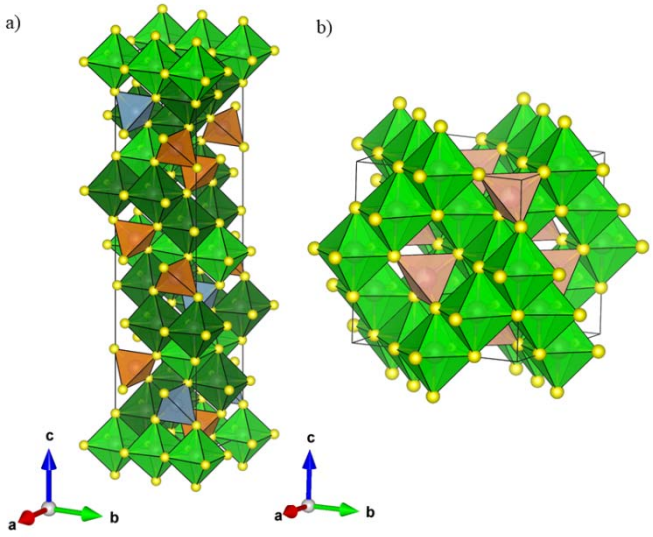

Figure 1. a) Crystal structure of β-In_2S_3. Ordered cation vacancies are located in Td(4a) sites (blue tetrahedra). In atoms are placed in Td(8e), Oh(8c), and Oh(16c) sites (orange tetrahedra, green and dark green octahedra). b) Crystal structure of α- In_2S_3. Fractional occupation of In atoms occurs in Td(8a) sites (light orange tetrahedra) coming from Td(8e) and Td(4a) sites of the β phase. Oh(8a) sites are fully occupied by In atoms.

On the other hand, α-In_2S_3 is a phase characterized by a single Td site, the Td(8a) site, which is shared by vacancies and In atoms as a consequence of the order-disorder transition taking place in In_2S_3 above 749 K. In other words, above that temperature vacancies spread over all Td(4a) and Td(8e) sites of the β phase and the structure changes from tetragonal to cubic with a single Td site in the structure.[18, 24-26] The cubic defect spinel phase was also observed in Al_2S_3 both when Al is partially substituted by a 2% As[27] and in Al_2S_3 and Al_2Se_3 at HP-HT conditions (4 GPa and 673 K).[23] The HT β-α phase transition (PT) in In_2S_3 has been revisited quite recently.[28] In addition, several recent studies have studied the β-α PT at ambient conditions.[29, 30] Aluminium substitution in β-In_2S_3 at relatively high concentration leads to chemical disordering between In and Al cations in the Td(8e) and Td(4a) sites and thus inducing the β-α PT.[29] On the other hand, an extensive study on the β-α PT has been carried out by playing with the composition, *x*, in $In_{1-x}Vac_xIn_2S_4$, where Vac stands for the vacancy.[30] This β-α PT has been induced by Se(Te)-for-S substitution as well.[31] Therefore, in view of these studies, the β-α PT can be triggered by HT or by composition.

Above 1100 K, another order-disorder transition occurs with vacancies being randomly distributed over both Td and Oh cation sites. This additional disorder thus leads to the γ phase,[24-26] that was refined by Pistor *et al.* during a reinvestigation of the HT PTs.[26] A few studies have considered the possibility of stabilizing γ-In_2S_3 at ambient conditions by adding a 5% of As, Sb, or Bi.[32, 33] The γ-phase of In_2S_3 is similar to the trigonal A-type phase of rare-earth sesquioxides, typical of La_2O_3; however, In atoms at the La 2d sites (z~0.25) of the La_2O_3 structure are splitted into two 2d sites of z~0.19 and 0.35 with fractional occupations in γ-In_2S_3. Noteworthy, the A-type phase of rare-earth sesquioxides was observed in In_2Se_3 at HT with a z~0.19,[34] so it is possible that the same phase is observed in γ-In_2S_3 and that problems with Rietveld refinement had yielded an additional 2d site with an abnormally high value of z (z~0.35).

HP studies in β-In_2S_3 have raised even more controversies than HT studies. The ε phase, with a corundum-like structure (S.G. *R*-3*c*, Z=6), was quenched from HP & HT studies (3.5 GPa and 800 K),[35] and this phase was also observed in Al_2S_3.[36] As regards HP studies carried out at ambient temperature, several X-ray diffraction (XRD) measurements have addressed the structural properties of the β phase under compression.[37-39] Three HP-PTs near 6.6, 11, and 35.6 GPa (the last one aided by laser heating) were reported by Lai *et al*.[37] The structure of the first two HP phases could not be determined, but the third one (hereafter named δ-In_2S_3) was identified as a defect Th_3P_4-like structure (S.G. *I*-43*d*, Z=5.33).[37] In agreement with Lai *et al.*, Yao *et al*. observed a HP-PT at 7.1 and 4.3 GPa in undoped and Ce-doped β-In_2S_3, respectively.[38] Concerning the 1st HP phase, they indexed it to a cubic structure, but no more details about the structure were given. Curiously, no HP-PT was found in a more recent HP-XRD work that studied β-In_2S_3 up to 41.3 GPa.[39] Despite this result, the same authors observed a pressure-induced metallization of In_2S_3 around 6.8 GPa in a later study;[40] a result that is in agreement with the first HP-PT seen in the two first HP-XRD studies. Finally, we must stress that the 1st HP-PT in β-In_2S_3 has been also recently evidenced by HP-Raman scattering (RS) and impedance spectroscopy measurements around 7 GPa.[41] Moreover, a semiconductor-metal PT at 41.2 GPa has been also reported.[41]

Despite the recent HP studies on β-In_2S_3, many questions are still open, being the most important ones related to the nature of the 1st and 2nd HP phases that remain unknown. On the other hand, no *ab initio* simulations of structural and vibrational properties of the β phase at HP have been conducted yet, to our knowledge, to help us to understand the obtained experimental results. Finally, neither of the already mentioned HP studies has explored if the β-α PT could be induced by pressure.

In this work, we present the results of a joint experimental and theoretical study on β-In_2S_3 under compression. HP-XRD and HP-RS measurements up to 15.0 and 21.2 GPa, respectively, are complemented with *ab initio* simulations to shed light on the above commented issues. We will show there are two HP-PTs whose onset is around 4.9 and 10.2 GPa. We will propose that the 1st HP phase has the cubic defect spinel structure (α-In_2S_3) and that the 2nd HP phase (hereafter named ϕ-In_2S_3) has a defect α-$NaFeO_2$-type structure. This is the first time, to our knowledge, that the defect α-$NaFeO_2$-type structure has been proposed as a post-spinel phase and the first time that it is commented on the possibility that the β-α PT could be induced by pressure. Moreover, we will show that the defect α-$NaFeO_2$-type structure bears a relation to the tetradymite-type structure, which is a typical structure of group-15 $B^{III}{}_2X^{VI}{}_3$ compounds

Please do not adjust margins

with topological insulating properties.[42] We will also provide an experimental and theoretical characterization of the structural and vibrational properties of the three phases (β, α, and ϕ). For this purpose, and due to the difficulty in simulating disordered structures, like α-In_2S_3 and ϕ-In_2S_3, we will discuss the properties of these two phases by comparison with isostructural compounds $CdIn_2S_4$ and Na(Ag)InS_2, respectively.

Most importantly, we will finally show in this work that thiospinels (either with $B^{III}{}_2X^{VI}{}_3$ or $A^{II}B^{III}{}_2X^{VI}{}_4$ composition) undergo pressure-induced order-disorder transitions similar to those of ordered-vacancy compounds. In other words, they tend to HP phases related to the NaCl structure, typical of *AX* or ABX_2 compounds (with the same number of cations and anions) as if vacancies could be counted as additional cations. Consequently, we will show that thiospinels at HP behave more similarly to ordered-vacancy compounds than to oxospinels and propose new experiments to verify it.

Experimental and theoretical details

β-In_2S_3 powders of high purity (99.999%) used in the present study were commercially acquired from Alfa Aesar company. Additionally, α-In_2S_3 powders of high purity (99.99%) were commercially acquired from Sigma Aldrich company. Powders were characterized at ambient conditions to verify the presence of either the β or the α phase. HP measurements on β-In_2S_3 at 300 K were performed using a membrane-type diamond-anvil cell (DAC) with 400 μm diameter culet. Powder samples were placed in a 150-μm diameter hole performed in a 40 μm-thick stainless-steel gasket and pressurized by a pressure-transmitting medium (PTM), like 4:1 methanol-ethanol mixture (M-E), that remains quasi-hydrostatic up to 10 GPa.[43, 44]

Angle dispersive powder HP-XRD measurements were carried out up to 15 GPa in BL04-MSPD beamline at ALBA synchrotron using a monochromatic X-ray beam with λ = 0.4246 Å and a Rayonix MARCCD detector located at 240 mm from the sample.[45] Copper was placed inside the pressure cavity and used as the pressure sensor through copper EoS[46], and a pinhole placed before the sample position was used as a cleanup aperture for filtering out the tail of the X-ray beam, which was focused down to 20 × 20 μm^2 using Kickpatrick-Baez mirrors. Powder XRD patterns were integrated as a function of 2θ using Dioptas software in order to obtain conventional, one-dimensional, diffraction profiles[47] that were refined using GSAS-II program package.[48]

Unpolarized HP-RS measurements were carried out up to 21 GPa using a Horiba Jobin Yvon LabRAM UV HR microspectrometer equipped with a thermoelectrically cooled multichannel charge coupled device detector that allows a spectral resolution better than 2 cm^{-1}. The Raman signal was excited with a HeNe laser (632.8 nm line) with a power of less than 10 mW and collected in backscattering geometry using an edge filter working in perpendicular configuration and cutting around 100 cm^{-1}. Raman signals down to 50 cm^{-1} or even less can eventually be detected by adjusting the angle between the edge filter and the light containing the Raman signal. The pressure was determined by the ruby luminescence method.[49] The frequencies of the Raman-active phonons were experimentally obtained by fitting Raman peaks with Voigt profiles of fixed Gaussian line width to the experimental setup resolution (1.6 cm^{-1}).[50, 51]

First-principles density-functional theory (DFT)[52] calculations at 0 K for β-In_2S_3, cubic spinel $CdIn_2S_4$, and $AgInS_2$ and $NaInS_2$ (both with α-$NaFeO_2$-type structure) were carried out with the Vienna Ab-initio Simulation Package (VASP),[53] using the projected augmented wave (PAW) scheme.[54, 55] Calculations were performed with the generalized gradient approximation (GGA) of Perdew-Burke-Ernzenhof revised for solids (PBEsol).[56] The basis set of plane waves was extended up to a cutoff 530, 600, and 530 eV for the β-In_2S_3, thiospinel $CdIn_2S_4$, and $AgInS_2$ and $NaInS_2$, respectively, in order to achieve highly converged results. For each relaxed structure, calculations were performed with the automatic k-point generation method included in the VASP package (Monkhorst-Pack scheme[57]) with Hellman-Feynman forces smaller than 0.004 eV/Å per atom and deviations of the stress tensor from the diagonal hydrostatic form smaller than 0.1 GPa.

Lattice dynamics calculations were performed at the zone center (Γ-point) of the Brillouin zone. The supercell method with the primitive cell was employed for the calculation of the dynamical matrix at the Γ-point.[53, 58] In order to obtain the phonon density of states at 0 GPa, a 2x2x2 supercell was used for β-In_2S_3 and $CdIn_2S_4$.

Structural search by theoretical means were employed to try to identify the 2nd HP crystalline structure phase of β-In_2S_3. The potential energy surface was systematically explored with the help of the minima hopping and evolutionary genetic methods. The first was employed in the multidimensional potential energy landscape of In_2S_3 with 5, 10, 15, 20, and 40 atoms in the unit cell. We have used the minima hopping method to identify the lower energy configurations at ambient pressure,[59, 60] and at least ninety symmetrically different local minima energy structures were identified for each cell size. The evolutionary genetic method was used as it is implemented in the USPEX code.[61-63] Initially, the first generation of prediction consisted of 300 structures by considering 1 to 10 formula units for fixed composition search in the unit cell. From the second generation onwards, structures were obtained by applying the 40% heredity (of each generation), 20% soft-mutation, and 20% transmutation operators. The remaining 20% of each generation was generated by using random[64] and topological generators.[65] This procedure was performed for 6 and 10 GPa pressure points, near those experimental transition observed. The structures predicted for both methods were kept according to their high symmetry, i.e., those with the least inequivalent atomic positions and a high number of symmetry operations. The study of partially occupied structures has been conducted with the Supercell program[66] to explore the different supercell configurations describing the analyzed structure. In this way, few theoretical XRD reflections and Raman modes are expected, as our HP-XRD and HP-RS measurements exhibit. For each method, each one of the selected structures was reoptimized with VASP and symmetrized by using similar convergence criteria than in the case of the vibrational analysis. Only those structures with the smallest energies and a few XRD peaks, like the ones obtained experimentally, were considered for further analysis.

Results and discussion

A. Structural properties under high pressure

Figure 2a) shows the evolution of the XRD patterns of β-In_2S_3 upon compression and decompression (d). For the sake of clarity, we have included the Miller indices (*h k l*) of the most intense reflections of the β phase at 0.9 GPa. An example of Le Bail refinement of the β phase at 0.9 GPa is shown in **Fig. 3**. At 4.9 GPa, most reflections of β phase occur. Only the most intense peaks of the β phase, namely, (1

Please do not adjust margins

0 3), (1 0 9), (2 0 6), (0 0 12), (3 1 8), (2 2 12), (2 2 15) and (4 0 8) reflections remain. Above 4.9 GPa, the β phase cannot be refined anymore; therefore, we consider that this is the onset transition pressure of the 1st HP-PT. Despite the PT, the Miller indices (*h k l*) of the β phase are used above 4.9 GPa to refer to the relevant reflections from the HP phases. Above 8.2 GPa, several weak reflections disappear (**Fig. 2**). At 10.2 GPa, the (1 1 6) reflection disappears and the relative intensities between the (1 0 9) and (2 0 6) reflections changes. Therefore, we consider that a 2nd HP-PT occurs above 10.2 GPa. On decompression down to 0.6 GPa, most of the reflections that disappeared during compression emerge again, thus pointing out the reversibility of the effect exerted by the pressure on β-In_2S_3.

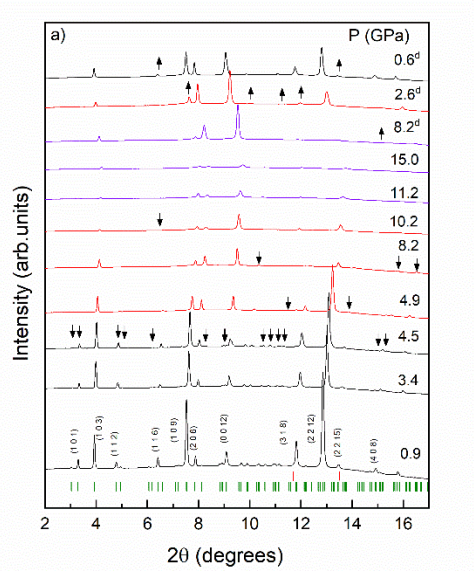

Figure 2. a) HP-XRD patterns of β-In_2S_3 on compression up to 15.0 GPa and decompression (d) down to 0.6 GPa. Labels for the most representative (h k l) indices for β-In_2S_3 are given. Green ticks represent the β-In_2S_3 reflections at the lowest pressure on upstroke. Black, red, and magenta colors represent the three β, α, and ϕ phases, respectively.

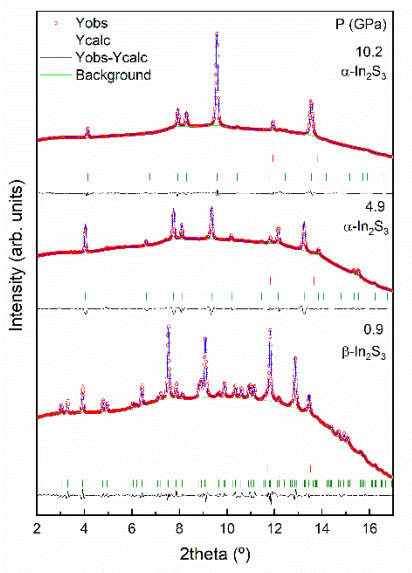

Figure 3. Le Bail refinement of selected XRD patterns of β-In_2S_3 at 0.9 GPa and of α-In_2S_3 at 4.9 and 10.2 GPa. Copper, β- and α-In_2S_3 reflections are marked with red, green and blue ticks, respectively.

Analysis of the structural parameters of β-In_2S_3 under compression has been obtained by LeBail refinement (see **Fig. 4**) and compared to those provided by theoretical calculations. A rather good agreement is found between the experimental and theoretical lattice parameters *a* and *c* and their evolution with pressure (**Fig. 4a)**). In fact, there is a better agreement of theoretical calculations with the *a* lattice parameter than with the *c* lattice parameter (that is slightly overestimated). Consequently, the theoretical volumes are slightly overestimated in comparison to experimental ones (**Fig. 4b)**). To evaluate the effect of pressure on the lattice parameters *a* and *c*, we have calculated the experimental (theoretical) zero-pressure axial compressibilities, defined as $\kappa_x = -\frac{1}{x}\frac{\partial x}{\partial P}$, which are: κ_a = 5.2·10^{-3} (6.2·10^{-3}) GPa and κ_c = 6.4·10^{-3} (6.7·10^{-3}) GPa. Our results show that the theoretical and experimental values for κ_c are closer than those for κ_a, unlike the case for the lattice parameters. Additionally, it is found that the long lattice parameter *c* is more compressible than the short lattice parameter *a*. This result can be understood if we consider that the ordered vacancies are placed along a 4_1 screw axis parallel to the *c* axis.

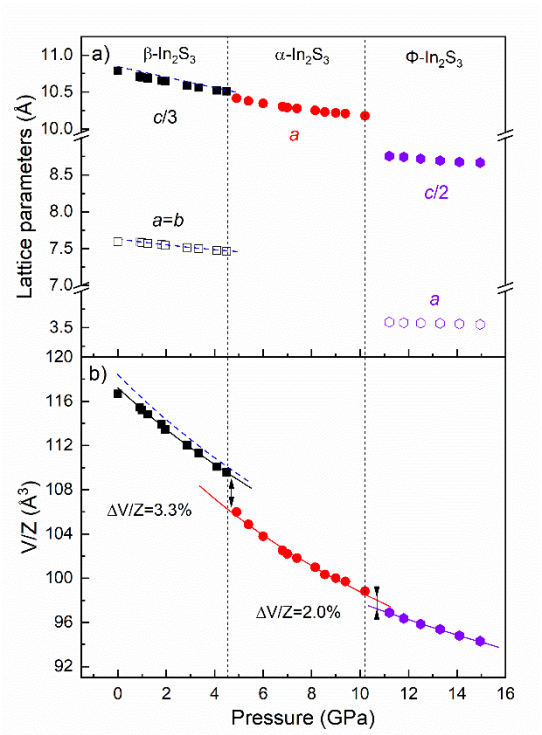

Figure 4. Pressure dependence of the lattice parameters (a) and volume per formula unit, V/Z (b), in β-, α-, and ϕ-In_2S_3. The theoretical pressure dependence of lattice parameters (dash lines) in β-In_2S_3 is plotted in a). Experimental (solid lines) and theoretical (dash lines) BM3-EoS for β-In_2S_3 are shown in b). Only experimental BM3-EoS (solid lines) are shown for α-, and ϕ-In_2S_3 in b).

To evaluate the experimental and theoretical pressure dependence of the unit-cell volume of the β phase, we have used both a 2nd and 3rd -order Birch-Murnaghan equation of state (BM2- and BM3-EoS). A good agreement between experimental and theoretical data and the corresponding BM3-EoS can be seen in **Fig. 4b)**. Our experimental

Please do not adjust margins

and theoretical zero-pressure volume (V_0), bulk modulus (B_0), and first pressure derivative (B_0') show a good agreement, as can also be seen in **Table 1**. Our B_0 values for β-In_2S_3 are very close to that reported for In_2S_3:Ce nanoparticles,[38] slightly smaller than those reported for In_2S_3 nanoparticles[38] and for bulk In_2S_3 in **Ref. 31** and larger than those reported for bulk In_2S_3 in **Ref. 39**. Again, the use of different PTMs and their associated hydrostatic limits[43] yield different values for B_0. In particular, our B_0 values are smaller than those of works using less hydrostatic PTM, like solid powders or silicon oil,[37, 38] and larger than those of works using equal or more hydrostatic PTM, like M-E and Ne.[39] In fact, we think that our results and those of **Ref. 39** are not so different. The main differences between the two works stem from the pressure range used to fit the EoS. In this work, the EoS was fitted up to 4.5 GPa, while in **Ref. 39** it was fitted up to 41.3 and 21.4 GPa, with M-E and Ne, respectively. It must be mentioned that the bulk modulus of β-In_2S_3 is similar to those of some OVCs, like α'-Ga_2S_3[67] and Ga_2Se_3,[68] and also similar to that of layered α-In_2Se_3 and β'-In_2Se_3.[69] In particular, the similar bulk modulus of an OVC, like β-In_2S_3, and of a layered material, like α-In_2Se_3, could be surprising since this last compound is a van der Waals compound that does not present vacancies in its structure; however, the gap between layers in van der Waals materials can be considered to be formed by intrinsic vacancies, as recently suggested,[70] and this justifies the similarities of both bulk moduli.

Table 1. Experimental (exp.) and theoretical (th.) unit-cell volume at zero pressure (V_0, in Å^3), bulk modulus (B_0, in GPa), and first pressure derivative (B_0') for β-In_2S_3. PTM used, and transition pressure (TP, in GPa) are also indicated. Results of previous HP works have been added for comparison.[37-39] The volume per formula unit (V/Z, in Å^3) for β-In_2S_3 (Z=16) is shown as well.

		V_0	B_0	B_0'	V/Z	TP	PTM
β-In_2S_3	exp.[b]	1876(2)	57(4)	4.5(7)	117(1)	4.9	M-E[a]
		1875(1)	58.2(7)	4.0, fixed	117(1)		
	th.[b]	1895.0(6)	53.1(9)	4.1(4)	118(1)		
		1895.0(4)	53.5(3)	4.0, fixed	118(1)		
	exp.[c]	1880.4[d]	37.8(2)	4.4(1)	118(1)	No TP	M-E[a]
		1882(1)	39.7(2)	4.0, fixed	118(1)		
		1880.4[d]	42.8(3)	4.1(1)	118(1)	No TP	Ne
		1883(1)	42.7(2)	4.0, fixed	118(1)		
	exp.[e]	1875(3)	63(3)	4.0, fixed	117(1)	6.6	S[a]
						6.8	LiF[f]
	exp.[g]	1880.7(1)	87(4)	4.0, fixed	118(1)	7.1	S[a]
		1918.1(1)	56(4)	4.0, fixed	120(1)	4.3[h]	
	exp.[i]					6.8	No PTM
	exp.[j]					~7.2	He
						6.8	No PTM

[a] M-E: 4:1 methanol-ethanol, S: silicone oil.
[b] Present work.
[c] **Ref. 39.**
[d] Authors in **Ref. 39** fix V_0 to 1880.4 Å^3 for the BM3-EoS for the different PTMs used.
[e] **Ref. 37**.
[f] No EoS is given in **Ref. 37**.
[g] **Ref. 38.**
[h] In_2S_3:Ce nanoparticles.
[i] **Ref. 40**. 1st PT observed by electrical measurements.
[j] **Ref. 41**. 1st PT observed by Raman and electrical measurements.

A deep analysis of the decrease of the relative volume of the different polyhedral units in β-In_2S_3, as provided by our theoretical calculations (**Fig. S1** in the Supplementary Information (SI)), shows that the small bulk modulus of β-In_2S_3 is mainly given by the compression of the polyhedral volume associated to the vacancy (Vac); i.e. the $VacS_4$ tetrahedron (centered at 4a sites). The In-based polyhedral units, InS_4 tetrahedra (centered at 8e sites) and InS_6 octahedra (centered at 8c and 16h sites), compress at a much smaller rate than the tetrahedron around the vacancy. BM2-EoS fit of polyhedral volumes yield a low bulk modulus (9.1 GPa) for the $VacS_4$ tetrahedron, which is much smaller than those for the InS_4 tetrahedron and InS_6 octahedra (8c and 16h sites), whose values are 54.8, 99.7, and 84.7 GPa, respectively. Therefore, the soft bulk modulus of β-In_2S_3 (~57 GPa) can be explained by the strong compression of the polyhedral unit around the vacancy. In fact, if one considers the polyhedral bulk moduli obtained from theoretical calculations and the multiplicity of each site in the tetragonal defect spinel structure, one can calculate a bulk modulus of ~65.5 GPa for β-In_2S_3, which is in relatively good agreement with the theoretical values for the bulk modulus obtained from the unit-cell volume (see **Table 1**).

A significant larger compression of the tetrahedron around the vacancy than of In-based polyhedra is noticed when comparing the theoretical Vac-S and In-S distances (**Fig. S2** in the SI). For the sake of completeness, we have also provided in **Fig. S3** in the SI the pressure dependence of the distortion index (D), quadratic elongation (λ), bond angle variance (σ^2), and effective coordination number (ECoN) corresponding to InS_4 and $VacS_4$ tetrahedra and both InS_6 octahedra in β-In_2S_3. Our calculations show a gradual change of all parameters with increasing pressure and, apparently, there is no abrupt change or singular value that could suggest the onset of the order-disorder PT taking place in β-In_2S_3 above 4.9 GPa.

We will now discuss the 1st HP phase observed above 4.9 GPa. The 1st PT is characterized by the disappearance of most reflections of the tetragonal defect spinel phase and the lack of appearance of new peaks; i.e. the β phase seems to be a superstructure of the 1st HP phase. Considering the group-supergroup relation between the α and β phases of In_2S_3, we considered the α phase with cubic spinel structure as a potential candidate for the 1st HP phase of the tetragonal β phase. In fact, we have successfully performed a LeBail refinement of XRD pattern of the 1st HP phase with the α phase from 4.9 to 10.2 GPa (see **Fig. 3**). For this purpose, we have used the structural data of the α phase from Pistor *et al.*[26] Above 10.2 GPa, the α phase does not fit the experimental XRD patterns anymore.

It is interesting to mention that the cubic spinel structure has also been observed in Al_2S_3, Al_2Se_3, $CdAl_2S_4$, $HgAl_2S_4$, $CdAl_2Se_4$, and $HgAl_2Se_4$ at HP-HT conditions (around 4-7 GPa and 673-873 K).[23, 71] Therefore, we consider that we have identified the nature of 1st HP phase of β-In_2S_3 and it corresponds to the cubic spinel structure. This phase is isostructural to α-In_2S_3, observed also at HT and under varying composition.

It must be stressed that in previous HP studies of β-In_2S_3 the nature of the 1st and 2nd HP phases could not be revealed. Indeed, our assignment of the 1st HP phase to the cubic α phase agrees with the cubic symmetry found for the 1st HP phase in a previous work (the S.G. was not provided).[38] The main difference between our work and **Ref. 38** is that our HP-XRD measurements at 4.9 GPa do not show the emergence of new peaks, unlike in **Ref. 38**. In this sense, we want to comment that the XRD patterns from **Ref. 38** do not exhibit a good peak resolution, likely due to the non-uniform nanoparticle size used in that study, so the appearance of new peaks close to those of the original phase must be considered with caution. It must also be noted that the disappearance of most of the weak reflections of the β phase was also observed in **Ref. 39**, despite the fact that no PT was claimed to occur in that study.

Please do not adjust margins

For the sake of comparison with the β phase, we have plotted the lattice parameter *a* (**Fig. 4a)**) and the volume per formula unit, V/Z, (**Fig. 4b)**) of α-In_2S_3 as a function of pressure. We must note that Z is 8 for a typical AB_2X_4 spinel; however, we must reformulate Z in terms of B_2X_3 stoichiometry, like β-In_2S_3, to compare the V/Z of the different phases studied. For this purpose, we have to consider the Td(8a) fractional occupation of 2/3 and the multiplicity of both In and S atoms. In this way, a renormalized Z=10.67 for the cubic spinel phase of α-In_2S_3 is obtained. By looking at the pressure dependence of V/Z for the β and α phases, we have observed a relative decrease of 3.3% at the 1st PT in β-In_2S_3. Curiously, this value is similar to the volume changes reported between the low pressure (LP) and HP phases of the AIn_2S_4 thiospinels.[72] This means that this small relative volume change seems to be typical of pressure-induced order-disorder PTs in both $B^{III}{}_2X^{VI}{}_3$ and $A^{II}B^{III}{}_2X^{VI}{}_4$ thiospinels.

The *a* lattice parameter compressibility, κ_a, of the α phase ($7.9 \cdot 10^{-3}$ GPa) is larger than those of the *a* and *c* axes of the β phase. On top of that, the bulk modulus, B_0, of the α phase (obtained either with BM2- or BM3-EoS, see **Table 2**) is smaller than that of the β phase (**Table 1**). The softer pressure behaviour of the α phase, reflected in its κ_a and B_0, is justified by the fractional occupation of the Td(8a) sites in the α phase, coming from ordered Td(8e) and empty Td(4a) sites in the β phase. An estimation of the unit-cell volume fraction associated with vacancies at 0 GPa yields a 1.54 and 3.22% for the β and α phases, respectively. These values reflect the larger fraction of the unit-cell volume occupied by vacancies in the α phase than in the β phase that supports the softer pressure behavior of the α phase compared to the β-phase. In this context, the disorder of cations and vacancies in the Td(8a) sites of the defect cubic spinel phase of α-In_2S_3 also explains its smaller B_0 in comparison with the cubic spinel phase of AIn_2S_4 compounds, that do not present vacancies in their occupied atomic positions (see **Table 2**).

Table 2. Experimental (exp.) unit-cell volume at zero pressure (V_0, in Å^3), bulk modulus (B_0, in GPa), and first pressure derivative (B_0') obtained for α-In_2S_3. Experimental and and theoretical (th.) data for the low-pressure (LP) and high-pressure (HP) defect-$LiTiO_2$-type phases of the AIn_2S_4 thiospinels (*A*=Cd, Mg, Mn) are given for comparison.[72] The volume per formula unit (V/Z, in Å^3) for α-In_2S_3 (Z=10.67), as well as for the spinel (Z=8) and defect-$LiTiO_2$-type (Z=8) phases of the AIn_2S_4 thiospinels are also shown. Note that the Z value of the defect-$LiTiO_2$ structure is renormalized to that of the typical AB_2X_4 composition of spinels. PTM used, and transition pressure (TP, in GPa) are indicated.

		V_0	B_0	B_0'	V/Z	TP	PTM
α-In_2S_3	exp.[b]	1245(9)	39(3)	4.5(8)	117(1)	8.2	M-E[a]
		1240(9)	42(3)	4.0, fixed	116(1)		
$CdIn_2S_4$	LP exp.[c]	1274(2)	78(4)	3.1(8)	159(1)	9.5	M-E[a]
	LP th.[c]	1241.45(2)	79.8(2)	4.65(6)	155(1)	11.5	
	HP exp.[c]	1206(6)	74(4)	4.0, fixed	151(1)		
	HP th.[c]	1174.6(8)	71.6(4)	4.0, fixed	147(1)		
$MgIn_2S_4$	LP exp.[c]	1227(1)	76.3(3)	2.8(7)	154(1)	8.3	M-E[a]
	LP th.[c]	1211.9(4)	75.4(9)	4.3(3)	152(1)	6.0	
	HP exp.[c]	1222(6)	55(2)	4.0, fixed	153(1)		
	HP th.[c]	1124.8(6)	68.8(4)	4.0, fixed	141(1)		
$MnIn_2S_4$	LP exp.[c]	1230(1)	78(4)	3.2(1)	154(1)	6.8	M-E[a]
	LP th.[c]	1200.7(5)	80(2)	3.9(3)	150(1)	6.9	
	HP exp.[c]	1187(2)	62(1)	4.0, fixed	148(1)		
	HP th.[c]	1121.0(4)	70.1(3)	4.0, fixed	140(1)		

[a] M-E: 4:1 methanol-ethanol, S: silicone oil.
[b] Present work.
[c] **Ref. [72].**

It must be noted that a smaller B_0 value of the 1st HP phase of the AIn_2S_4 (*A*= Cd, Mn, Mg) thiospinels, with defect $LiTiO_2$ structure, than that of the cubic spinel phase has also been observed (**Table 2**).[72] Again, this is a result of the pressure-induced order-disorder PTs. In the cubic spinel phase of AIn_2S_4 thiospinels, all cations are mainly ordered with *A* cations occupying Td(8b) sites and In cations occupying Oh(16c) sites. However, in the defect $LiTiO_2$ structure, *A* and In cations are disordered in the Oh(16c) sites, resulting in a larger compressibility than that of the cubic spinel phase.

Further support to the assignment of the 1st HP In_2S_3 phase to the α phase comes from the value of the lattice parameter *a* of the α phase extrapolated to 0 GPa: *a*= 10.758 Å (10.745 Å) from our BM3-EoS (BM2-EoS). This value compares well with the lattice parameter *a* of 10.736 Å obtained from the commercial sample powders of α-In_2S_3 at ambient pressure (see **Fig. S4a)** in the SI). These values can be nicely compared with data reported in the literature for the α phase. In fact, a value of *a*= 10.774 Å was reported many years ago at ambient conditions,[18] and a little bit longer lattice parameter *a* of 10.832 Å was refined at 749 K.[26] Moreover, the α phase was observed with a lattice parameter *a* of 10.769 and 10.758 Å in $In_{1-x}Vac_xIn_2S_4$ with In contents of 40.5 and 41.0 %, respectively.[30] As observed, these values of the lattice parameter *a* for the α phase match quite well with our experimental values, thus confirming the nature of the 1st HP phase of β-In_2S_3.

As already commented, the β-α PT that is induced by HT or varying composition yields the mixing of the ordered Td(8e) and empty Td(4a) sites in the β phase within a unique disordered Td(8a) site in the α phase. Considering that 2/3 of Td positions in the β phase (the Td(8e) sites) are occupied when these sites mix with the empty Td(4a) sites, the occupation fraction in Td(8a) sites in the α phase must be 2/3. This is confirmed in the studies of HT[24-26] and it is also expected for HP since no change of composition is expected in either HT or HP studies. Unfortunately, we cannot provide the occupation fraction of Td(8a) sites in the α phase obtained at HP due to the impossibility to perform Rietveld refinements of our HP-XRD patterns. In this context, it must be noted that the α phase obtained by introducing a high In content exhibit an occupation fraction in the Td(8a) site that is higher than 2/3,[30] in opposition with what is observed at HT and is expected at HP. This reasoning allows us to predict that a slightly higher bulk modulus of the α phase should be observed in $In_{1-x}Vac_xIn_2S_4$ samples with a high content of In than in stoichiometric α-In_2S_3. In fact, this hypothesis is indirectly supported by the smaller values of the lattice parameter *a* found in $In_{1-x}Vac_xIn_2S_4$ samples with a high content of In[30] with respect to samples of almost stoichiometric α-In_2S_3,[18] if one considers the typical inverse relationship between volume and bulk modulus. Therefore, the results on $In_{1-x}Vac_xIn_2S_4$ samples give support to our assignment of the nature of the 1st HP phase in β-In_2S_3.

Now, we will focus on the 2nd HP phase observed above 10.2 GPa. First of all, we want to remember that a 2nd PT was reported above 11 GPa in **Ref. 37**. In that work, the 2nd PT was identified by the emerging of new peaks at about 2.6 and 3.0 Å of *d* spacing, but the nature of the 2nd HP phase was not identified perhaps due to the lack of an enough number of diffraction peaks and because of the weakness of the few peaks observed.[37] It must be noted that the new peaks observed in **Ref. 37** should be located around 8 and 9 degrees in our XRD patterns, near the (2 0 6) and (0 0 12) reflections of the previous β phase, respectively. Curiously, no new peaks appear near these reflections appear in our HP-XRD measurements. On the other

Please do not adjust margins

Please do not adjust margins

hand, the HP-XRD patterns of **Ref.** [39] show the disappearance of the (1 1 6) reflection as well as the change in the relative intensity of (1 0 9) and (2 0 6) reflections of the previous β phase, as occurs in our HP-XRD patterns (**Fig. 2** and **3**). Therefore, we can conclude that the results of **Ref. 39** provide evidence of the 2nd PT, despite the authors of **Ref.** [39] said that no PTs were observed in their HP-XRD measurements.

To identify the 2nd HP phase of β-In_2S_3, several approaches have been undertaken. First, we tried with several polymorphs observed on In_2S_3 either at HP, at HT, or at HP-HT. They include the ε phase, the γ phase, and the δ phase.[37] Moreover, LP and HP phases seen in other compounds with *AX* (NaCl, CrB, LuS, TlS, CoO and NiO), ABX_2 ($LiTiO_2$, $LiFeO_2$ and $NaFeO_2$), A_2X_3 (Gd_2S_3, U_2S_3, Th_2S_3, Os_2Al_3 and In_2Se_3), ABX_3 (perovskite, post-perovskite), and AB_2X_4 (post-spinel $CaMn_2O_4$, $CaTi_2O_4$ and $CaFe_2O_4$) compositions have been tested. Further to this, we decided to use structure prediction methods to help us obtain the crystalline structure of the 2nd HP phase of β-In_2S_3. After all this challenging task, we found that the rhombohedral α-$NaFeO_2$-type (S.G. *R*-3*m*, Z=3) structure, a layered distorted variant of the NaCl-type structure[73] observed in ABX_2 compounds,[74-78] was the only one compatible with our XRD patterns. LeBail refinements of the 2nd HP phase with a defect α-$NaFeO_2$-type structure at two pressures (11.2 and 15 GPa) are plotted in **Fig. 5**. This 2nd HP phase (ϕ-In_2S_3) is also a defective phase with vacancies and cations mixed at the same Wyckoff sites and has a smaller number of reflections than those in α-In_2S_3. In particular, the peak located around 6.8 degrees in α-In_2S_3 (**Fig. 3**) disappears in ϕ-In_2S_3 (**Fig. 5**). Furthermore, the notable widening of the peaks located around 8.5 and 13.8 degrees around 15 GPa (**Fig. 5**) comes from the splitting of many reflections of ϕ-In_2S_3.

Figure 5. Le Bail refinement of selected XRD patterns of ϕ-In_2S_3 at 11.2 and 15.0 GPa. Copper and ϕ-In_2S_3 reflections are marked with red and purple ticks, respectively.

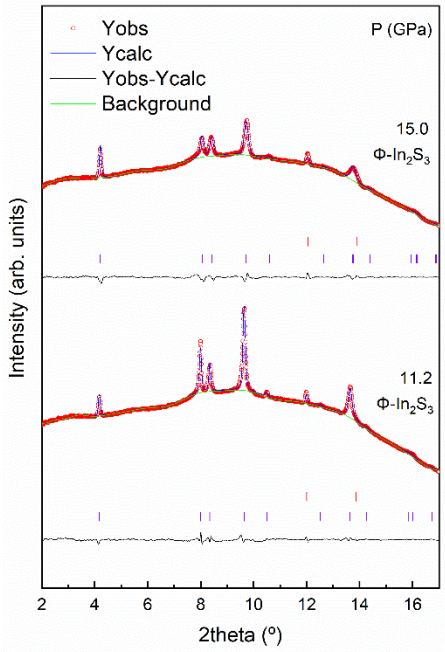

We must stress that this is the first time, to our knowledge, that a post-spinel phase with defect α-$NaFeO_2$-type structure has been proposed. Noteworthy, this phase has been obtained by chemical lithiation of spinel $LiTi_2O_4$[79] and in spinel $LiCoO_2$ at HT.[80] Additionally, the spinel structure is also found in high-energy irradiated α-$NaFeO_2$.[81] These are clear examples of the relation between the rhombohedral *R*-3*m* α-$NaFeO_2$-type structure of ABX_2 compounds and the cubic *Fd-3m* spinel structure of AB_2X_4 compounds. On top of that, the α-$NaFeO_2$-type structure has been found at ambient conditions in several $B^{III}{}_2X^{VI}{}_3$ compounds, like Sc_2S_3,[82] Ti_2S_3[83] and Zr_2Se_3.[84] These last compounds have 2 equal octahedra in 3a and 3b sites for the *B* cation and an occupation fraction of 1/3 in the 3b sites. Due to the lack of Rietveld refinements, we propose for ϕ-In_2S_3 the same occupation observed in the above mentioned $B^{III}{}_2X^{VI}{}_3$ compounds with this α-$NaFeO_2$-type structure (see **Fig. 6a)**); i.e., a full occupation of 3a sites by In atoms and a 1/3 occupation of 3b sites by In atoms. For the sake of comparison, we have included the structure of $NaInS_2$ (**Fig. 6b)**), where Na cations are in those sites where the ϕ-In_2S_3 has 1/3 of occupation fraction. In conclusion, we propose the defect α-$NaFeO_2$-type structure as the 2nd HP phase of ϕ-In_2S_3 at ambient temperature.

Figure 6. Comparison of ϕ-In_2S_3 a), α-$NaFeO_2$ b), and α-Bi_2Te_3 c) structures. Note that vacancies have been added at 3b sites (those between the layers) in the tetradymite structure of α-Bi_2Te_3 to highlight the similitudes the α-$NaFeO_2$-type and tetradymite-type structures.

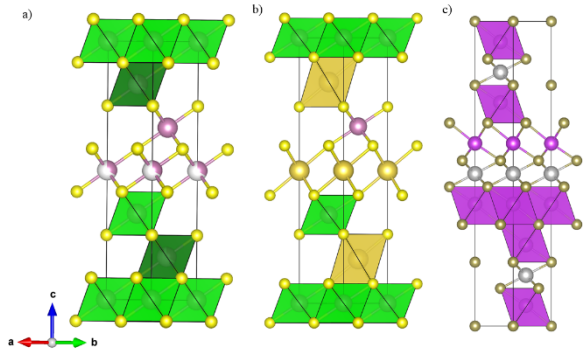

Curiously enough, if we remove 1 of every 3 cation layers (from partially occupied 3b sites) of the defect α-$NaFeO_2$-type structure (S.G. *R*-3*m*), we can obtain the tetradymite-like structure (also S.G. *R*-3*m*) observed in many $B^{III}{}_2X^{VI}{}_3$ compounds, like Bi_2Se_3 (**Fig. 6c)**). In this way, the structural relation between the defect $NaFeO_2$-type structure and tetradymite structure is emphasized. In a recent work, it has been proposed that the array of intrinsic vacancies forming the gap between the layers in van der Waals materials, like those having a tetradymite structure, should be considered as part of the crystalline structure.[70] If we apply this rule, both structures are even more connected. In this way, it seems that for $B^{III}{}_2X^{VI}{}_3$ compounds with *B* cations in octahedral coordination, like in the NaCl-type structure, some cations that mix well with vacancies can lead to the defect α-$NaFeO_2$-type structure, like in Sc_2S_3, while other cations that do not mix well with vacancies can lead to the tetradymite-like structure, like in Bi_2Se_3, where atoms and vacancies group into separate planes leading to quintuple layers.

For the sake of comparison with the previous phases, we have plotted the lattice parameters *a* and *c* (**Fig. 4a)**) and the volume per formula unit, V/Z, (**Fig. 4b)**) of ϕ-In_2S_3 as a function of pressure. Again, reformulating Z for ϕ-In_2S_3 we got Z=2 by considering the occupation fraction of 1/3 in the 3b sites and the multiplicity of both In and S atoms. Attending to the pressure dependence of V/Z for the α and ϕ phases, a relative volume decrease of 2.0% at the 2nd PT in β-In_2S_3 is obtained. Again, this value is similar to the volume changes

Please do not adjust margins

Please do not adjust margins

reported between the LP and HP phases of the AIn_2S_4 thiospinels,[72] so this result confirms that this small relative volume change seems to be typical of pressure-induced order-disorder PTs in both $B^{III}{}_2X^{VI}{}_3$ and $A^{II}B^{III}{}_2X^{VI}{}_4$ thiospinels.

The *a* and *c* lattice parameter compressibilities, κ_a and κ_c, of the ϕ phase ($3.1\cdot10^{-3}$ and $5.4\cdot10^{-3}$ GPa, respectively) are smaller than those of the *a* and *c* axes of the β phase and than that of the *a* axis of the α phase. On top of that, the bulk modulus, B_0, of the ϕ phase (obtained either with BM2- or BM3-EoS, see **Table 3**) is larger than those of the β and α-phases. Note that the unit-cell volume fraction associated with vacancies in the ϕ phase is ~11.11 %; i.e. larger than those in the β and α phases, but this does not result in a softer pressure behaviour of the ϕ phase than the other two phases. The harder pressure behaviour of the ϕ phase is not justified by its fractional occupation of 1/3 in the octahedral cation 3b sites, but for the smaller compressibility of octahedra than of tetrahedra in all spinel-related structures. In addition to this, the low V/Z of the ϕ phase (109 $Å^3$ (Z=2)) in comparison to those of β and α phases (117.25 (Z=16) and 116.68 (Z=10.67) $Å^3$, respectively) support the largest incompressibility of the ϕ phase. It must be stressed that the experimental bulk modulus found for ϕ-In_2S_3 is like the theoretical ones predicted for isostructural $AgInS_2$, with a similar V value, and larger than $NaInS_2$, with a larger V value (see **Table 3**). This result is in good agreement with the already mentioned inverse relation between volume and bulk modulus.

Table 3. Experimental (exp.) unit-cell volume at zero pressure (V_0, in $Å^3$), bulk modulus (B_0, in GPa), and first pressure derivative (B_0') obtained for ϕ-In_2S_3. Theoretical (th.) data for $NaInS_2$ and $AgInS_2$ are given for comparison. The volume per formula unit (V/Z, in $Å^3$) for ϕ-In_2S_3 (Z=2) and Na(Ag)InS_2 (Z=3) are shown as well.

		V_0	B_0	B_0'	V/Z
ϕ-In_2S_3	exp.	217(3)	78(3)	4.4(4)	109(1)
		216(3)	82(4)	4.0, fixed	108(1)
$NaInS_2$	th.	248.9(1)	51(5)	4.6(7)	83(1)
		247.8(4)	56(2)	4.0, fixed	83(2)
$AgInS_2$	th.	229.6(2)	86(2)	4.8(2)	77(1)
		229.2(3)	93(2)	4.0, fixed	76(1)

B. Vibrational properties under high pressure

For β-In_2S_3, containing 16 molecules in the unit cell, group theory predicts the 120 vibrational modes at the Brillouin zone center:

$$\Gamma = 9\,A_{1g} + 5\,A_{1u} + 4\,A_{2g} + 11\,A_{2u} + 9\,B_{1g} + 5\,B_{1u} + 4\,B_{2g} + 11\,B_{2u} + 17\,E_u + 14\,E_g$$

From these modes, there are 3 acoustic modes ($A_{2u} + E_u$) and 117 optic modes that correspond to 42 infrared-active modes (10 A_{2u} + 16 E_u), 50 Raman-active modes (9 A_{1g} + 9 B_{1g} + 4 B_{2g} + 14 E_g), and 25 silent modes (5 A_{1u} + 4 A_{2g} + 5 B_{1u} + 11 B_{2u}) that are all hyper-Raman-active except for the 4 A_{2g} modes. Therefore, 36 Raman-active and 26 IR-active peaks are expected since E_g modes (as well as E_u modes) are doubly degenerated. A superindex has been added to the symmetry of the vibrational modes of the different phases to classify them as a function of increasing frequency.

Fig. 7a) shows a selection of HP-RS spectra of β-In_2S_3 under compression up to 21.2 GPa and decompression (d) down to ambient pressure. The Raman modes of the β phase disappear above 4.5 GPa; i.e. at the onset of the 1st PT in good agreement with our HP-XRD measurements. When this PT occurs, the relatively narrow Raman peaks of the β phase disappear, and eight broad bands appear that are consistent with the disorder of cations and vacancies in tetrahedral sites, as expected for the α phase. Moreover, the Raman intensity of most peaks lowers noticeably (at about a 25% of the β phase's signal). For that reason, selected normalized Raman spectra from 5.6 to 21.2 GPa are shown in **Fig. 7b)**. Above 8.6 GPa, the Raman signal becomes even worse (at about a 10% of the β phase's signal), and only two broad bands can be distinguished. This marks the onset of the 2nd PT that is in good agreement with our HP-XRD measurements. Finally, upon decompression from 21.2 GPa, we observed several broad bands, as during upstroke, and the appearance of the main Raman modes of the β phase below 1.2 GPa; thus supporting the partial reversibility of the two observed PTs. This result is again in good agreement with our HP-XRD measurements.

Figure 7. a) Stacked Raman spectra of β-In_2S_3 under compression up to 21.2 GPa and under decompression down to ambient pressure b) Normalized Raman spectra under compression in the range of 5.0 and 21.2 GPa, where HP phases α-In_2S_3 and ϕ-In_2S_3 are seen. Up and down arrows in both panels show the Raman peaks that disappear/emerge under both compression and decompression.

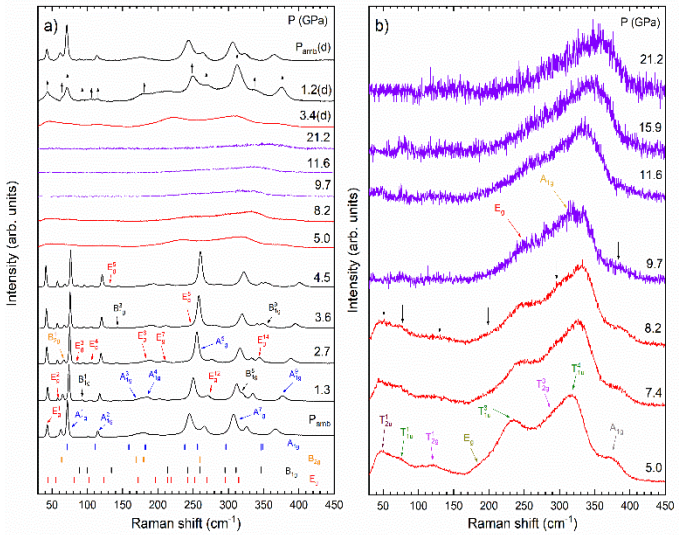

The Raman spectrum of β-In_2S_3 at ambient conditions (see the bottom Raman spectrum of **Fig. 7a)**) is similar to that published in previous works.[30, 41, 85-87] The Raman spectrum covers a wide range (between 40 and 400 cm^{-1}) and shows similar features to those reported by Kambas *et al.*[85] Moreover, our Raman spectra at different pressures are in agreement with those already found in previous HP-RS measurements.[41] However, unlike in **Ref. 41**, we have measured a considerable frequency shift of the Raman-active modes of β-In_2S_3 (see **Fig. 8** and **Table 4**), especially for the high-frequency modes. These Raman shifts do not agree with the almost negligible Raman shifts reported in **Ref. 41** for both hydrostatic and non-hydrostatic HP-RS measurements. The experimental and theoretical pressure dependence of the frequencies corresponding to the Raman-active modes of the β phase are plotted in **Fig. 8**. The good agreement between the experimental and theoretical zero-pressure Raman frequencies and their pressure coefficients has allowed us to tentatively assign the symmetry of the 22 observed Raman-active modes of the β phase (see **Fig. 7** and **Table 4**). With the exception of the B_{1g}^2 mode, we have assigned all the predicted modes to every

Please do not adjust margins

observed peak below 120 cm^{-1}. At higher frequencies, the assignment is more doubtful due to the large number of Raman-active modes of the β phase and the lack of clear observation of a number of them. It can be noticed that, in general, the pressure coefficient of the frequency of the Raman-active modes increases as the frequency increases (see **Table 4**). The two lowest frequencies E_g modes (near 50 cm^{-1}) show negative pressure coefficients, while the modes above 300 cm^{-1} show the highest-pressure coefficients. In particular, the E_g^{13} mode exhibits the highest theoretical pressure coefficient (10.1 cm^{-1}GPa^{-1}).

Figure 8. Pressure dependence of the experimental (symbols) Raman frequencies of β-, α-, and ϕ-In_2S_3 during compression. For comparison with experimental data of the three phases, theoretical (lines) for β-In_2S_3, $CdIn_2S_4$, and $NaInS_2$ have been plotted.

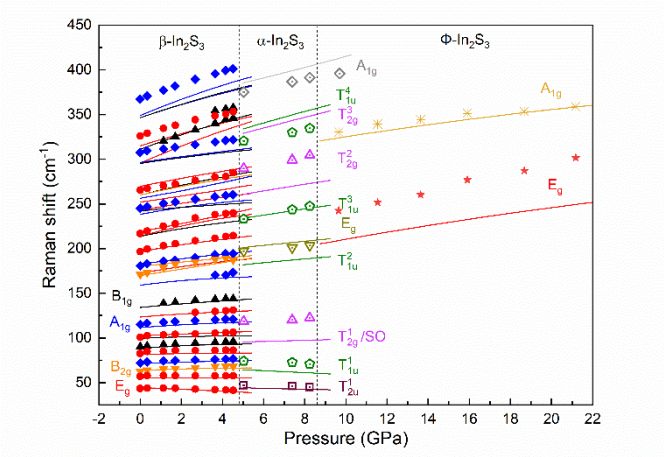

Table 4. Theoretical (th.) and experimental (exp.) Raman-active frequencies at zero pressure (ω_0, in cm^{-1}) and pressure coefficients (a_1, in cm^{-1}·GPa^{-1}; a_2, in 10^{-2} cm^{-1}·GPa^{-2}) in β-In_2S_3 according to fits to $\omega_0 + a_1P + a_2P^2$.

	β-In_2S_3 th.			β-In_2S_3 exp.		
Mode	**ω_0**	**a_1**	**a_2**	**ω_0**	**a_1**	**a_2**
E_g^1	44.4(1)	-0.9(1)	-3(1)	44(1)	-0.3(2)	-6(4)
E_g^2	55.4(1)	-0.02(1)		58(1)	-0.06(1)	
B_{2g}^1	63.6(1)	1.0(1)	-9(1)	63(2)	2.1(3)	-20(6)
A_{1g}^1	71.2(1)	0.9(1)	-5(1)	73(2)	1.1(2)	-6(3)
E_g^3	81.5(1)	0.6(1)	-5(2)	85(3)	0.8(3)	-9(6)
B_{1g}^1	88.5(1)	1.6(1)	-14(1)	90(3)	2.0(2)	-16(4)
B_{1g}^2	99.5(1)	0.9(1)	-6(1)			
E_g^4	102.2(1)	1.1(1)	-4(2)	102(3)	1.0(2)	-3(4)
A_{1g}^2	111.6(1)	1.8(2)	-11(3)	115(2)	2.0(2)	-16(5)
E_g^5	123.4(1)	1.9(1)	-11(2)	125(3)	1.3(1)	
B_{1g}^3	134.1(1)	2.1(1)	-6(2)	135(3)	4.0(1)	-34(8)
A_{1g}^3	159.0(1)	3.0(1)	-23(1)	156(4)	3.0(2)	
B_{2g}^2	169.7(2)	3.7(2)	-2(4)			
E_g^6	172.4(1)	4.0(1)	-19(2)	171(4)	8.0(1)	-88(20)
B_{2g}^3	179.9(2)	2.6(2)	-6(4)			
A_{1g}^4	182.5(1)	3.2(1)	-10(2)	182(4)	4.0(1)	-15(10)
E_g^7	196.5(2)	4.1(2)	-15(5)	197(4)	5.0(1)	-35(10)
B_{1g}^4	213.8(2)	4.6(2)	-22(4)			
E_g^8	214.0(1)	6.3(1)	-33(3)	217(4)	8.1(4)	-64(10)
E_g^9	219.0(3)	4.3(4)	7(7)			
A_{1g}^5	238.2(3)	4.4(4)	-27(5)	245(2)	4.4(2)	-23(4)
B_{1g}^5	242.1(2)	2.1(3)	-7(5)			
E_g^{10}	242.8(2)	4.1(3)	-10(5)			
E_g^{11}	252.0(2)	3.3(2)	4(3)			
A_{1g}^6	256.3(1)	3.9(1)	13(1)			
B_{1g}^6	259.9(1)	5.8(1)	-19(2)			
B_{2g}^4	260.1(2)	5.1(3)	-18(5)			
E_g^{12}	269.7(2)	4.7(2)	-12(4)	266(2)	4.0(1)	6(20)
B_{1g}^7	295.3(2)	3.5(2)	-12(4)			
E_g^{13}	295.6(3)	10.1(4)	-28(7)			
A_{1g}^7	296.3(2)	3.4(2)	-8(3)	308(2)	3.4(3)	-7(6)
B_{1g}^8	311.1(2)	8.6(2)	-25(4)	311(3)	9.0(1)	-23(13)
E_g^{14}	315.0(4)	7.2(4)	-20(7)	326(2)	7.8(3)	-43(7)
B_{1g}^9	346.9(1)	5.9(2)		340(4)	3.9(1)	
A_{1g}^8	346.5(3)	7.8(3)	-23(6)			
A_{1g}^9	348.7(3)	9.8(3)	-33(6)	367(2)	9.1(2)	-36(3)

The spread of the theoretical and experimental Raman-active modes along the frequency axis and the increasing pressure coefficients of such modes with increasing frequency in β-In_2S_3 (**Fig. 8**) is similar to those observed in many OVCs, like Ga_2S_3,[67] $CdGa_2S_4$,[88] $HgGa_2S_4$,[89] $ZnGa_2Se_4$,[90] $CdGa_2Se_4$,[91] $HgGa_2Se_4$,[92] $CdAl_2S_4$,[93] and $CdIn_2Se_4$.[94] However, these OVCs exhibit phonon gaps between low-frequency modes (with negligible or negative pressure coefficients) and high-frequency modes (with positive pressure coefficients) that are not observed in β-In_2S_3. As can be observed in **Fig. S5a)** in the SI, the one-phonon density of states (PDOS) of β-In_2S_3 only has a unique narrow phonon gap below 280 cm^{-1}. The reason for the lack of a phonon gap in β-In_2S_3, unlike in other OVCs, could be related to the existence of 4- and 6-fold coordinated In atoms in β-In_2S_3, in contrast to other OVCs, whose cations are only 4-fold coordinated. We must recall that the stretching and bending modes of InS_6 octahedra have smaller frequencies than those of InS_4 tetrahedra because of the more considerable In-S bond distances in the octahedra than in the tetrahedra. Therefore, the lower frequencies of the bending modes of the octahedra that will extend in the region below 200 cm^{-1} allow explaining the lack of the phonon gap in β-In_2S_3, unlike in tetrahedrally-coordinated OVCs. Another relevant difference between β-In_2S_3 and tetrahedrally-coordinated OVCs is the lack of the breathing mode of the vacancy in the Raman spectrum of β-In_2S_3. This mode is usually the strongest peak of the Raman spectrum in tetrahedrally-coordinated Ga-based OVCs, and it is also notably strong in $CdIn_2Se_4$ near 133 cm^{-1}.[94] Thanks to our lattice dynamics calculations and with the use of the J-ICE visualizer,[95] we have found that the breathing mode in β-In_2S_3 is the B_{2u}^9 silent mode at 296.86 cm^{-1}. The silent nature of this mode explains why the breathing mode is entirely absent in the Raman spectrum of β-In_2S_3.

Regarding the 1st PT, we must comment that the related abrupt change observed in the Raman spectrum at 5.0 GPa (**Fig. 7a)**) has also been reported at a slightly higher pressure (around 6.5 GPa) in previous HP-RS measurements with different PTM.[41] In particular, four broad Raman bands were reported between 6.5 and 10 GPa in the Raman spectra under hydrostatic (He as PTM) and non-hydrostatic conditions (no PTM).[41] Therefore, we conclude that existing HP-RS measurements confirm the existence of this 1st PT in agreement with HP-XRD measurements.

Let us now comment about the vibrational modes of the 1st HP phase. For the cubic spinel structure, one expects 42 vibrational modes at the Γ point. These modes result in 5 Raman-active (A_{1g}+ E_g + 3 T_{2g}), 4 IR-active (4 T_{1u}), and 4 silent (2 A_{2u} + 2 T_{2u}) modes, with *E* and *T* modes being doubly and triply degenerated, respectively.[96] Due to the inverse cation distribution in AIn_2S_4 thiospinels; i.e. disorder between 4-fold coordinated *A* cations and 6-fold coordinated In atoms, a partial breakdown of the Raman selection rules occurs due to the loss of translation symmetry, and IR-active and silent modes could be observed in the Raman spectrum.[97] Therefore, a total of 13 modes could be observed in the Raman spectrum of α-In_2S_3. We have measured 8 modes in the Raman spectrum of the 1st HP phase (see **Fig. 7b)**). The frequencies and pressure coefficients of the 8 modes measured and assigned to α-In_2S_3 are summarized in **Table 5**. The pressure coefficients were

Please do not adjust margins

obtained from the experimental data fitting to the equation $\omega_0 + a_1(P - P_0)$, with P_0 = 5.0 GPa.

The fractional occupation in the Td(8a) sites of α-In_2S_3 complicates the simulation of its structural and vibrational properties. Therefore, in order to help assigning the symmetry of the experimentally observed modes of the α phase, we have tabulated in **Table 5** the theoretical and experimental[98] modes of $CdIn_2S_4$ thiospinel, as an approach to the observed modes of α-In_2S_3. That approximation is justified by the similarity of Cd and In masses and by the proximity of the molecular masses of both compounds per unit cell: 3763 and 3474 for $CdIn_2S_4$ (Z=8) and α-In_2S_3 (Z=10.66), respectively. Therefore, similar vibrational frequencies would be expected for both compounds at similar pressures. With this information, we have tentatively assigned the modes observed in the Raman spectrum obtained from the commercial sample powders of α-In_2S_3 at ambient pressure (**Fig. S4b)**) and at HP in **Fig. 7b)**. For a better comparison, the Grüneisen parameter for each vibrational mode, $\gamma = B_0 \cdot a_1/\omega_0$, is used to normalize the pressure coefficients of the modes observed in both α-In_2S_3 and $CdIn_2S_4$ (see **Table 5**). Since the value of B_0 for $CdIn_2S_4$ is almost twice that for α-In_2S_3 (see **Table 2**), γ'values for $CdIn_2S_4$ are almost twice those for α-In_2S_3 (see **Table 4**).

Table 5. Experimental (exp.) zero-pressure frequencies (ω_0, in cm^{-1}), pressure coefficients (a_1, in $cm^{-1}\cdot GPa^{-1}$; a_2, in 10^{-2} $cm^{-1}\cdot GPa^{-2}$) and Grüneisen parameters, $\gamma = B_0 \cdot a_1/\omega_0$ (ω_0 at 0 GPa), of the observed modes in α-In_2S_3 as obtained from fits of Raman data to $\omega_0 + a_1(P - P_0)$, with P_0 = 5.0 GPa. Frequencies of α-In_2S_3 from commercial powders and from extrapolations of HP data are also given for comparison. Also summarized are theoretical (th.) and experimental zero-pressure frequencies, pressure coefficients, and reduced slopes of Raman-, IR- and silent-active modes in $CdIn_2S_4$. The theoretical data of $CdIn_2S_4$ have been fitted to $\omega_0 + a_1 P$. To calculate γ, we have used B_0= 39 GPa for α-In_2S_3 and 79.8 GPa for $CdIn_2S_4$ and the frequencies measured at 0 GPa.

	α-In_2S_3 (exp.)[a]					$CdIn_2S_4$ (th.)[a]			$CdIn_2S_4$ (exp.)[b]		
Mode	ω_0[c]	a_1	γ	ω_0[d]	ω_0[e]	ω_0	a_1	γ	ω_0	a_1	γ
T_{2u}^1 (S)	48(2)	-0.5(2)	-0.4(2)	49(3)	43(1)	49.5(3)	-0.9(1)	-1.5(2)			
T_{1u}^1 (IR)	74(2)	-1.0 (1)	-0.5(2)	79(3)	70(1)	69.4(3)	-1.1(1)	-1.2(2)	70(1)	0.7(2)	0.8(3)
T_{2g}^1 (R)	119(2)[f]	1.1(2)	0.4(3)	113(1)	110(1)	92(1)	0.7(1)	0.6(1)	93(1)	0.5(2)	0.4(3)
T_{1u}^2 (IR)						169.7(2)	2.6(1)	1.0(2)			
A_{2u}^1 (S)						185.0(2)	1.6(1)	0.7(1)			
E_g (IR)	198(3)	1.9(3)	0.4(1)	187(2)	185(1)	189.1(2)	2.3(1)	1.0(1)	188(1)	2.7(2)	1.1(1)
T_{1u}^3 (IR)	236(3)	4.5(1)	0.8(1)	210(3)	217(1)	216.4(3)	3.5(4)	1.3(1)	207(1)	2.6(2)	1.0(1)
T_{2u}^2 (S)						227.7(3)	3.8(1)	1.3(1)			
T_{2g}^2 (R)						241.5(4)	3.7(1)	1.2(1)	249(1)	4.4(2)	1.4(1)
T_{2g}^3 (R)	291(3)	5(1)	0.7(2)	270(2)	264(1)	299.7(4)	6.0(1)	1.6(2)	315(1)	5(2)	1.2(1)
T_{1u}^4 (IR)	323(3)	4.4(3)	0.6(2)	298(2)	305(1)	301.2(1)	3.5(2)	1.7(1)	301(1)	3.3(2)	0.9(1)
A_{2u}^2 (S)					341(1)	354(1)	6.2(1)	1.4(1)			
A_{1g} (R)	378(3)	5(1)	0.6(2)	354(3)	370(1)	357(1)	5.8(1)	1.3(1)	360(1)[g] 367(1)[h]	6.1(2)[g] 6.1(2)[h]	1.3(1)[g] 1.3(1)[h]

[a]Present work.
[b]**Ref. 98**.
[c]Frequencies of α-In_2S_3 at 5.0 GPa (from data fitting).
[d]Frequencies of α-In_2S_3 at 0 GPa (extrapolated from fits to HP data).
[e]Frequencies of α-In_2S_3 at 0 GPa (experimental data from commercial α-In_2S_3).
[f]This mode can be assigned either the T_{2g}^1 symmetry or as a second order (SO) mode. Further details in the text.
[g]A_{1g} mode associated with the vibration of InS_4 tetrahedral units, according to **Ref. 98**.
[h]A_{1g} mode associated with the vibration of CdS4 tetrahedral units, according to **Ref. 98**.

According to our experimental results on α-In_2S_3 and the comparison with isostructural $CdIn_2S_4$, the bands observed in the Raman spectrum of α-In_2S_3 at ambient pressure (**Fig. S4b)**) can be explained as follows (see **Table 5**). The first band located at 43 cm^{-1} should correspond to a silent T_{2u}^1 mode that is calculated to be around 49.5 cm^{-1} in $CdIn_2S_4$. A negative value of γ is observed for this mode in α-In_2S_3 and also predicted in $CdIn_2S_4$. This T_{2u}^1 mode is neither Raman- nor IR-active and becomes Raman-active due to the cation-vacancy disorder in the T_d(8a) sites of the α phase. Concerning the T_{2u}^2 and A_{2u}^1 modes, their theoretical ω_0 do not compare well with those observed experimentally in our HP-RS measurements (**Table 5**). On top of that, they cannot be assigned properly the Raman spectra of the commercial α-In_2S_3 powders of Sigma Aldrich at ambient pressure because of the broad band between 150 and 250 cm^{-1} (**Fig. S4b)**). However, we have tentatively assigned the A_{2u}^2 mode, the highest-frequency silent mode, to the right shoulder of that peak located at about 300 cm^{-1} (**Fig. S4b)**). The band at about 70 cm^{-1} can be assigned to the IR-active T_{1u}^1 mode, with a_1 quite close to that calculated for $CdIn_2S_4$ and both with negative γ. Curiously, the experimental pressure coefficient of this mode in $CdIn_2S_4$ was found to be of opposite sign to that of calculations.[66] This soft mode was also observed in $MgIn_2S_4$,[98], while in $MnIn_2S_4$, the T_{1u}^1 mode was not observed. The T_{1u}^2 mode, not observed either in α-In_2S_3 or in $CdIn_2S_4$, should be located around 170 cm^{-1}, in accordance with our calculations for $CdIn_2S_4$. The T_{1u}^3 and T_{1u}^4 modes in α-In_2S_3 have been assigned to the broad peaks located in our Raman spectra around 217 and 305 cm^{-1} (236 and 323 cm^{-1} near 5 GPa in **Fig. 7b)**), by means of the agreement among the a_1 and ω_0 of our α-In_2S_3 (those extrapolated at 0 GPa, see **Table 5**) and both experimental and theoretical ones of the $CdIn_2S_4$. Furthermore, these T_{1u}^3 and T_{1u}^4 modes can be likely associated with the peaks observed around 237 and 306 cm^{-1} near 6.6 GPa in **Ref. 41**, but the a_1 reported in **Ref. 41** for these modes do not match with those collected in our **Table 5**. The γ values for the T_{1u}^3 mode in α-In_2S_3 and $CdIn_2S_4$ are the highest below 230 cm^{-1}. Regarding the T_{1u}^4 mode, the experimental and theoretical γ values in α-In_2S_3 and $CdIn_2S_4$, respectively, are the highest above 230 cm^{-1}.

The rest of the broad bands seen in the Raman spectra of the commercial α-In_2S_3 sample at ambient pressure and in the 1st HP phase of β-In_2S_3 are tentatively attributed to Raman-active modes of α-In_2S_3. The broad bands located around 110 and 264 cm^{-1} at ambient pressure (119 and 291 cm^{-1} near 5 GPa in **Fig. 7b**) can be assigned to the T_{2g}^1 and T_{2g}^3 modes. It must be stressed that the T_{2g}^1 could also be assigned as a second-order mode, as Ursaki *et al.* assigned for the mode observed with a zero-pressure frequency around 110 cm^{-1} in $CdIn_2S_4$.[98] On the other hand, we consider that the T_{2g}^2 mode is not observed in our Raman spectra of α-In_2S_3. This mode should be placed between 249 and 285 cm^{-1}, where the ω_0 of $CdIn_2S_4$, $MgIn_2S_4$, and $MnIn_2S_4$ thiospinels are placed for this mode.[98] On the other hand, we have assigned the broad peak located around 185 cm^{-1} at ambient pressure (198 cm^{-1} around 5 GPa in **Fig. 7b**) to the E_g mode on the basis of the close values of the experimental and theoretical a_1 and ω_0 in $CdIn_2S_4$, which are also in agreement with those experimental a_1 reported for the $MgIn_2S_4$ and $MnIn_2S_4$ thiospinels.[98] In addition, positive γ values are observed in α-In_2S_3 for this E_g mode, as well as in AIn_2S_4 thiospinels.[98] Last but not least, we have tentatively assigned the highest-frequency broad peak placed around 370 cm^{-1} at ambient pressure (378 cm^{-1} around 5 GPa in **Fig. 7b**) to the A_{1g} mode, according to the experimental and theoretical a_1 and ω_0 in $CdIn_2S_4$. This A_{1g} mode can also be assigned to the broad band observed near 373 cm^{-1} around 7 GPa in **Ref. 41**. As was stressed by Ursaki *et al.*[98], the A_{1g} mode refers to the breathing mode (In-S symmetric stretching of InS_4); i.e. the vibration of S atoms towards the centre of the tetrahedron. This mode splits into two

Please do not adjust margins

Please do not adjust margins

bands in inverse AIn$_2$S$_4$ thiospinels, associated with the S motion in AS$_4$ and InS$_4$ tetrahedra due to cation disorder. The pressure evolution of these two bands has been experimentally seen in the HP-RS measurements of AIn$_2$S$_4$ thiospinels, and this mode was found to have one of the highest values of the pressure coefficients,[98] in good agreement with our HP-RS measurements in α-In$_2$S$_3$. Similarly, the A_{1g} mode must also split in α-In$_2$S$_3$, due to the cation-vacancy disorder at Td(8a) sites, between the S motions of VacS$_4$ and InS$_4$. Unfortunately, we do not presently know the location of such a local vibrational mode if it exists.

A final comment can be added regarding the pressure coefficients of the β and α phases. It can be observed that the Raman modes with the smallest frequencies in both phases show negative pressure coefficients, unlike in ϕ-In$_2$S$_3$ (see **Fig. 7a)**). The negative pressure coefficients of the low-frequency modes in both phases are due to the softening of zone-edge TA phonons in tetrahedrally bonded solids that is not present in octahedrally bonded solids.[99] Some of these zone-edge phonons become Raman active due to zone folding of cubic structures in more complex structures with a smaller group symmetry, like in β-In$_2$S$_3$, or with a large number of atoms in the unit cell, like in α-In$_2$S$_3$. Therefore, the negative pressure coefficient of the lowest frequency mode in the 1st HP phase of β-In$_2$S$_3$ is a direct proof that tetrahedral coordination is still present in that phase, and thus gives support to our assignment of the 1st HP phase of β-In$_2$S$_3$ to the cubic spinel structure of α-In$_2$S$_3$ where In cations are both tetrahedrally and octahedrally coordinated as in β-In$_2$S$_3$.

Support for the identification of the 1st HP phase of β-In$_2$S$_3$ with α-In$_2$S$_3$ also comes from the matching between the Raman- and IR-active modes observed in the 1st HP phase of β-In$_2$S$_3$ and those seen in α-In$_2$S$_3$ thin films deposited on different substrates,[41-43] as well as in quenched α-In$_2$S$_3$ samples with high In contents.[30] For example, the lowest-frequency IR-active T_{1u}^1 mode has been observed weakly on cubic In$_2$S$_3$ thin films deposited on InAs substrates[100] and in quenched α-In$_2$S$_3$ samples with higher In contents.[30] The modes found in several works around 126, 240, and 266 cm^{-1} at ambient pressure can be tentatively assigned to T_{2g}^1, T_{1u}^3, and T_{2g}^2 modes (the last one not observed in our HP-RS measurements). These frequencies have been traditionally attributed to the presence of α-In$_2$S$_3$ on annealed In$_2$S$_3$ thin films deposited on glass substrates.[101, 102] A broad band observed near 166 cm^{-1} on In$_2$S$_3$ thin films[100] could be attributed to the T_{1u}^2 mode (not seen in our Raman spectra), which could also be consistent with the modes reported around 170 and 178 cm^{-1} in quenched α-In$_2$S$_3$ samples with In content of 41.0 and 41.5%, respectively.[30] In these quenched samples, the modes around 206 and 211 cm^{-1} found in samples with In content of 41.0 and 41.5%, respectively, could be related to the E_g mode at 200 cm^{-1} in our α-In$_2$S$_3$ sample at ambient pressure . Finally, the high-frequency modes T_{2g}^3, T_{1u}^4, and A_{1g} mode can be seen in In$_2$S$_3$ thin films and in quenched α-In$_2$S$_3$ samples with a high In contents above 295 cm^{-1}.[30, 100-103] All in all, the vibrational information provided in this work for the 1st HP phase of β-In$_2$S$_3$ gives support to its α-In$_2$S$_3$ nature.

Finally, we have included the theoretical PDOS of CdIn$_2$S$_4$ at 0 GPa in **Fig. S5b)** in the SI, as an approach to that of α-In$_2$S$_3$, in order to compare the vibrational properties of α-In$_2$S$_3$ and β-In$_2$S$_3$. As observed, the narrow phonon gap of β-In$_2$S$_3$ located at 280 cm^{-1} (**Fig. S5a)** becomes wider in the α phase (**Fig. S5b)**). Furthermore, a second-wide phonon gap appears around 340 cm^{-1}. Curiously, the Raman spectra of the α phase under compression (**Fig. 7b)**) and that measured from the commercial powders of α-In$_2$S$_3$ (**Fig. S4b**) do not seem to show those two phonon gaps. In this context, we can speculate that perhaps the cation-vacancy disorder in Td(8a) sites in the α phase results in broad Raman bands that prevent the observation of such phonon gaps in the Raman spectrum.

As regards the 2nd HP phase of β-In$_2$S$_3$, we have already commented that above 8.2 GPa most Raman modes of the α phase disappear, and only three broad bands are observed (see **Fig. 7**). In fact, one of these modes corresponds to the A_{1g} mode of the α phase that persists up to 9.7 GPa. Therefore, only two broad bands between 200 and 350 cm^{-1} can be ascribed to the 2nd HP phase above 8.2 GPa (see **Fig. 7b)**). According to group theory, the rhombohedral α-NaFeO$_2$-type phase has 12 vibrational modes at the Γ point with irreducible representations:

$$\Gamma = 1A_{1g}(R) + 2A_{2u}(IR) + 1E_g(R) + 2E_u(IR) + 1A_{2u} + 1E_u$$

where R and IR indicate the Raman- and IR-active modes. Therefore, there are 2 Raman-active modes (E_g and A_{1g}), 4 IR-active modes ($2A_{2u}$ and $2E_u$), and 3 acoustic modes. The two Raman-active modes correspond to anion movements in the stretching and bending modes of the cation-anions bonds.[74] The frequency shifts of the two bands of ϕ-In$_2$S$_3$ upon compression up to 21.2 GPa are plotted in **Fig. 8**. Of these two peaks, the smallest (highest) in frequency was previously followed under pressure up to 23 (43) GPa.[41] In this respect, our HP-RS measurements agree with those already published.[41] The main difference between both HP-RS studies is that the previous work does not consider that there is a PT above 8.6 GPa, despite there are clear changes in the Raman spectra supporting this 2nd PT in β-In$_2$S$_3$.

To verify that the two observed Raman bands of the 2nd HP phase of β-In$_2$S$_3$ correspond to the *R*-3*m* structure of defect α-NaFeO$_2$, we have simulated the pressure dependence of the Raman-active frequencies of isostructural NaInS$_2$ as an approach to the observed modes of ϕ-In$_2$S$_3$ (see **Fig. 8** and **Table 6**). That approximation is justified by the proximity of the molecular masses of both compounds per unit cell: 620 and 656 for NaInS$_2$ (Z=3) and ϕ-In$_2$S$_3$ (Z=2), respectively. Therefore, similar vibrational frequencies are expected for both compounds at similar pressures. With this information, we have tentatively assigned the modes observed in the Raman spectrum of ϕ-In$_2$S$_3$ above 8.2 GPa in **Fig. 7b)**, whose pressure dependence of the vibrational frequencies are plotted in **Fig. 8**.

For a better comparison of ϕ-In$_2$S$_3$ and NaInS$_2$, the Grüneisen parameter for each vibrational mode, $\gamma = B_0 \cdot a_1 / \omega_0$, is used to normalize the pressure coefficients in both compounds (see **Table 6**). A good agreement between the extrapolated experimental frequencies of ϕ-In$_2$S$_3$ at ambient pressure and the experimental[74] and theoretical frequencies of NaInS$_2$ at ambient pressure can be observed. Moreover, both compounds show similar a_1 and γ values (see **Table 6**). This result gives support to the assignment of the 2nd HP phase of β-In$_2$S$_3$ to the defect α-NaFeO$_2$-type structure. Therefore, we can conclude that our HP-RS measurements provide clear support for the existence of two pressure-induced order-disorder PTs in tetragonal β-In$_2$S$_3$ up to 20 GPa. Besides, Raman spectra of the 1st and 2nd HP phases are consistent with the cubic spinel (α-In$_2$S$_3$) and the defect α-NaFeO$_2$-type (ϕ-In$_2$S$_3$) structures, respectively, as suggested by Le Bail refinements of our HP-XRD measurements.

Please do not adjust margins

Please do not adjust margins

Table 6. Experimental (exp.) zero-pressure frequencies (ω_0, in cm^{-1}), pressure coefficients (a_1, in $cm^{-1}\cdot GPa^{-1}$; a_2, in 10^{-2} $cm^{-1}\cdot GPa^{-2}$) and Grüneisen parameters, $\gamma = B_0\cdot a_1/\omega_0$ (ω_0 at 0 GPa), of the observed modes in ϕ-In_2S_3 as obtained from fits of Raman data to $\omega_0 + a_1(P - P_0) + a_2(P - P_0)^2$. Also summarized are theoretical (th.) zero-pressure frequencies, pressure coefficients, and Grüneisen parameters of the Raman-active modes in $NaInS_2$ with α-$NaFeO_2$ structure. The theoretical data of $NaInS_2$ have been fitted to $\omega_0 + a_1P + a_2P^2$. To calculate γ we have used B_0= 78 GPa for ϕ-In_2S_3 and 51 GPa for $NaInS_2$.

	ϕ-In_2S_3 (exp.)				$NaInS_2$					
Mode	**ω_0[a]**	**a_1**	**a_2**	**γ**	**ω_0[b]**	**ω_0[c]**	**a_1[c]**	**a_2[c]**	**γ[c]**	**ω_0[d]**
E_g	242(2)	5(1)	1(7)	1.6(2)	195(5)	165.1(2)	5.1(1)	-5.0(2)	1.5(1)	158
A_{1g}	331(1)	4(1)	-14(4)	0.9(2)	279(5)	284.6(2)	4.6(1)	-5.1(2)	0.8(1)	289

[a] Frequencies of ϕ-In_2S_3 at 9.7 GPa (from data fitting).

[b] Frequencies of ϕ-In_2S_3 at 0 GPa (extrapolated from fits to HP data).

[c] Values for the $NaInS_2$ obtained from our theoretical calculations.

[d] Experimental frequencies of $NaInS_2$ at ambient conditions from **Ref. [78]**.

To finish this section, we want to stress that the defect α-$NaFeO_2$ structure bears a close relation with the defect $LiTiO_2$ structure found as a HP phase in AIn_2S_4 (*A*=Cd, Mg, Mn) thiospinels. It must be noted that two broad Raman peaks were also observed in the HP phase of AIn_2S_4 (*A*=Cd, Mg, Mn) thiospinels,[98] as it occurs in the 2nd HP phase of β-In_2S_3. In both kinds of thiospinels, a drastic decrease of the Raman signal was observed at the PT (**Fig. 5a)**). In the case of AIn_2S_4 thiospinels, a defect NaCl-type structure (typical HP phase of $A^{II}B^{III}{}_2X^{VI}{}_4$ OVCs) and later observed in $CdAl_2S_4$,[93] was first proposed as a HP phase from HP-RS measurements.[98] However, subsequent HP-XRD measurements determined that the HP phase of AIn_2S_4 (*A*=Cd, Mg, Mn) thiospinels was a defect $LiTiO_2$-type structure.[72] In this context, it must be stressed that both $LiTiO_2$ and α-$NaFeO_2$ structures are typical phases of ABX_2 compounds and that both structures derive from the NaCl-type structure, with all cations in octahedral coordination. The main difference between both structures is that in cubic $LiTiO_2$ cations are alternated in the sequence *A-X-B-X* along the different spatial directions, much like the NaCl structure, while in rhombohedral α-$NaFeO_2$ different types of cations and anions are grouped in different layers in a sequence *A-X-B-X*, thus resulting in the formation of a layered structure with atomic planes perpendicular to the *c* axis of the hexagonal unit cell. It may be speculated that the different arrangement of cations in these two structures can be related to the different size of the cations (Li and Ti have similar ionic radii, while Na and Fe have rather different ionic radii). Following this line of reasoning, the different ionic radii of In, on one hand, and the average of the mixture of an In atom and two vacancies, on the other hand, could be responsible for the different behaviour at HP of In_2S_3 with respect to AIn_2S_4 (*A*=Cd, Mg, Mn) thiospinels.

C. Structural stability of β-In_2S_3 at high pressure and pressure-induced PTs

Let us now discuss the stability of β-In_2S_3 under compression based on the information provided in this and previous HP works, as summarized in **Table 1**, and the implications of the pressure-induced PTs found in β-In_2S_3.

Clearly, our measurements show two PTs up to 20 GPa for the β phase. Our first transition pressure (~4.8 GPa according to our HP-XRD and HP-RS measurements) is in agreement with that observed in In_2S_3:Ce nanoparticles[32] and smaller than those reported in In_2S_3 nanoparticles[32] and in In_2S_3 powders.[37, 40, 41] We assume that the difference in transition pressures between different works comes from the different PTM and techniques employed since in many previous HP works, rather non-hydrostatic PTMs have been used, especially considering the softness of an OVC such as β-In_2S_3.

On the other hand, results from **Ref. [39]** are more controversial since no PTs were detected with different PTM, despite the fact that we consider that the two PTs were observed in **Ref. [39]**. According to **Fig. 2** in **Ref. [39]**, the (1 1 2) reflection disappears and the (1 1 6) decreases sharply at about 5.1 GPa with M-E (run-1), meanwhile both reflections disappear at 5.9 GPa with Ne (run-2). The same feature occurs in our HP-XRD measurements at 4.9 GPa (**Fig. 2**), thus supporting the observation of the first PT in **Ref. [39]**. On the other hand, it must be stressed that in Fig. 3 of **Ref. [39]**, peaks corresponding to *d spacing* values greater than 5.0 Å are not reported. Above this value, the weak (0 0 4) peak, observed at 3.03 degree at 0.9 GPa, as well as the (1 0 1) and (1 0 3) reflections can be observed in **Fig. 2a)**. In fact, the (1 0 3) peak is observed at 0.4 GPa in **Fig. 1** of **Ref. [39]**, but not the (0 0 4) and (1 0 1) peaks. In this context, it is important to notice that both (0 0 4) and (1 0 1) reflections disappear at 4.9 GPa, and only the (1 0 3) reflection remains in our HP-XRD measurements at that pressure (**Fig. 2**). Besides, the disappearance of some reflections was observed in **Ref. [39]** below 5.0 Å (**Figs. 3 a)** and **b)** of **Ref. [39]**) for run-1 and run-2 at 5.1 and 5.9 GPa, respectively, as occurs in our HP-XRD measurements at 4.9 GPa (**Fig. 2 a)**). Noteworthy, the same authors from **Ref. [39]** performed electrical measurements under HP in **Ref. 38,** where they reported a semiconductor-metal transition at 6.8 GPa by electrical measurement that is likely related to the vacancy disorder occurring in β-In_2S_3 at the first PT. In this respect, it is also noticeable that the HP-RS measurements from **Ref. 39** evidenced an abrupt change in the Raman modes at 7.2 and 6.8 GPa, with He and without PTM, respectively. Therefore, the β phase is not stable under compression between 4.8 and 6.8 GPa. In conclusion, we can confirm, on the basis of the similarities between our HP-XRD measurements and those from **Ref. [39]**, that the first PT is well observed in our HP-XRD measurements and also in earlier HP works.[37, 38, 40, 41]

The existence of phase transitions in β-In_2S_3 below 20 GPa is further confirmed by our theoretical simulations of the energy vs volume and relative enthalpy vs pressure between β-In_2S_3 and ϕ-In_2S_3 (see **Fig. S6a)** and **S6b)**, respectively, in the SI). Clearly, the simulated ϕ-In_2S_3 shows an enthalpy smaller than β-In_2S_3 above 5 GPa. This result is consistent with the α-ϕ PT observed above 8.2 GPa. The disordered ϕ-In_2S_3 could be simulated due to few possible supercells (only 7 combinations) suggested by Supercell program.[66] However, the number of possible supercells to simulate α-In_2S_3 is computationally prohibitive ($2.3\cdot10^{13}$), so no simulation of this phase has been performed.

We also want to comment on the reversibility of the pressure effects on β-In_2S_3. In agreement with our HP-XRD measurements at 0.6 GPa on dowstroke from 16 GPa (**Fig. 2a)**), our HP-RS measurements below 1.2 GPa on downstroke from 21 GPa also show the appearance of β-In_2S_3 (**Fig. 5a)**). The reversibility of β-In_2S_3 was already commented in a previous HP-RS work.[35] In that work, the β phase was recovered when the pressure was relaxed from 8.6 and 7.8 GPa, with He and without PTM, respectively; however, the β phase was not recovered from 43.0 GPa in both runs. This lack of reversibility of β-In_2S_3 from pressures beyond 40 GPa does not match with the reversibility observed by HP electrical measurements up to 41.6

Please do not adjust margins

GPa.[40] Therefore, we can conclude that the different PTMs used and the compression/decompression rates seem to provide different conditions that influence in the reversibility of the pressure-induced PTs in β-In_2S_3.

It must be stressed that the two observed PTs we have observed up to 20 GPa seem to be reversible under suitable conditions. The reversibility of pressure-induced PTs was also found in AIn_2S_4 thiospinels,[72] but not in pseudocubic $CdIn_2Se_4$.[94] The reversibility of the pressure-induced PTs of β-In_2S_3 is very interesting since α-In_2S_3 is a metastable phase at ambient conditions, which is even sold by Sigma Aldrich company, and it could be potentially retained upon decompression from pressures above 12 GPa (once the PT to the 2nd HP phase of β-In_2S_3 is completed). As already commented, the β phase was not recovered on decreasing pressure from 43.0 GPa in **Ref. [41]**; however, the Raman spectrum at ambient pressure of our commercial α-In_2S_3 sample (**Fig. S4b)**) and that obtained at ambient pressure on downstroke in **Ref. [41]** are rather similar. Both show a broad band between 150 and 380 cm^{-1} that has a maximum near 300 cm^{-1} and two shoulders near 200 and 350 cm^{-1}. Therefore, we think that the sample recovered from 43.0 GPa in **Ref. [41]** corresponds to a very disordered or amorphous α-In_2S_3 structure. We consider that this recovered sample has disorder also at anion sites because the bands near 300 and 350 cm^{-1}, corresponding to S vibrations, are much broader in the Raman spectrum of the recovered sample in **Ref. [41]** than in the Raman spectrum of commercial α-In_2S_3. Therefore, we can conclude that the pressure-induced PTs of β-In_2S_3 are reversible from 20 GPa, but are not reversible from 40 GPa. In the last case, a disordered or amorphous α phase can be recovered, which is in good agreement with the nature of the 1st HP phase of β-In_2S_3 we have reported.

Finally, we want to comment that this work has complemented previous HP works on $B^{III}{}_2X^{V}{}_3$ and $A^{II}B^{III}{}_2X^{VI}{}_4$ compounds and has found a new nexus between thiospinels and tetrahedrally-coordinated OVCs of these two families of compounds. In particular, it has been found that thiospinels undergo pressure-induced order-disorder PTs either to the defect NaCl structure (typical of *AX* compounds and tetrahedrally-coordinated OVCs), like $CdAl_2S_4$,[93] or to defect $LiTiO_2$ and defect α-$NaFeO_2$ structures (two distorted NaCl-type structures typical of ABX_2 compounds), like thiospinel AIn_2S_4 compounds (A= Cd, Mg, and Mn)[72] and In_2S_3, respectively.

In any case, the previous statement is far from being completely proved and more studies need to be conducted. For instance, on the basis of HP-RS measurements, $ZnAl_2S_4$ thiospinel has been proposed to undergo a PT towards the $CaFe_2O_4$ structure, as many oxospinels.[104] On the other hand, an alternative sequence of pressure-induced PTs related to corundum has been recently predicted for Al_2S_3 up to 200 GPa.[105] In particular, a PT from the tetragonal defect spinel ($I4_1/amd$) to corundum (R-3c) and then to the *Pbcn* structure of In_2O_3 at HP[106] have been proposed for Al_2S_3. Therefore, this work prompts to carry out HP-XRD measurements on Al_2S_3 and spinel $ZnAl_2S_4$ to prove whether the post-spinel phase of these thiospinels is a defect NaCl-related phase, a $CaFe_2O_4$ phase, or a corundum-type phase.

Conclusions

We have revisited the pressure behavior of β-In_2S_3 with tetragonal defect spinel structure using HP-XRD and HP-RS measurements. Our measurements have been supported by *ab* initio calculations to evaluate the effect of pressure on the stability of this interesting OVC. As a result, we have observed two pressure-induced PTs above 5.0 and 10.5 GPa, respectively. The 1st PT is a first-order PT characterized by a 3.3% decrease of the relative volume per formula unit and corresponds to the order-disorder β-α PT. The 2nd PT is a first-order PT characterized by a 2.0% decrease of the relative volume per formula unit and corresponds to the α-ϕ PT. Curiously, the α phase (cubic spinel) exhibits a lower bulk modulus than the β phase due to the larger fraction of vacancies in the volume per formula unit in the α than in the β phase. Furthermore, this disorder also explains the smaller bulk modulus of α-In_2S_3 than those of isostructural AIn_2S_4 thiospinels (*A*=Cd, Mg, Mn).

After an extensive search through phases of materials with *AX*, ABX_2, B_2X_3 and AB_2X_4 composition, we have proposed that the 2nd HP phase of β-In_2S_3 (ϕ-In_2S_3) has the defect α-$NaFeO_2$-type structure. This structure is a derivative of the NaCl-type structure typical of ABX_2 compounds. This is the first time that this structure has been found as a post-spinel phase, to our knowledge. ϕ-In_2S_3 is less compressible than β- and α-In_2S_3 because it has vacancies in octahedrally coordinated positions that are less compressible than vacancies in tetrahedrally coordinated sites, as it occurs in β- and α-In_2S_3.

From the vibrational perspective, the β-α PT is characterized by an abrupt change in the Raman spectra. A decrease in the number of peaks, a considerable broadening of the peaks, and a much smaller Raman intensity were observed. On the other hand, the α-ϕ PT is characterized by a reduction in the number of broad bands from 8 to 2 and further decrease of the Raman intensity. Thanks to our lattice-dynamic calculations and their good agreement with our experimental results, we have tentatively assigned the symmetry of the experimentally observed Raman modes of the β phase. Moreover, we have assigned the symmetry of the experimentally observed Raman modes of the α phase by comparison with the calculated Raman-, IR-, and silent-active modes of isostructural $CdIn_2S_4$ as an approach to α-In_2S_3. Similarly, we have assigned the symmetry of the experimentally observed Raman modes of the ϕ phase by comparing them with the calculated Raman-active modes of isostructural $NaInS_2$ as an approach to ϕ-In_2S_3. Moreover, our identification of the α phase as the 1st HP phase of β-In_2S_3 is supported by the comparison of the XRD and RS measurements of commercial α-In_2S_3 powder samples at ambient pressure.

As regards the reversibility of the pressure-induced PTs, both our HP-XRD and HP-RS measurements show the reversibility of the changes induced by applying pressure on β-In_2S_3 up to 21 GPa. Moreover, we have shown that previous HP measurements on β-In_2S_3 up to 40 GPa are consistent with the recovery of strongly disordered or amorphous α-In_2S_3 at ambient pressure. In summary, the present work proposes for the first time: i) that α-In_2S_3 is accessible from the stable β phase not only by HT or by varying composition, but also at HP, and that it can be recovered from HP experiments under suitable conditions, and ii) that a defect α-$NaFeO_2$-type structure can be another post-spinel phase in thiospinels.

Finally, we have shown that our present work represents an important complement to previous HP works in thiospinels. In particular, we have evidenced that many cubic group-13 thiospinels undergo pressure-induced phase transitions to defect NaCl related structures (defect $LiTiO_2$ and defect α-$NaFeO_2$), which are typical of *AX* and ABX_2 compounds (with the same number of cations and anions). Since pressure-induced PTs to the defect NaCl structure are

Please do not adjust margins

common in tetrahedrally-coordinated OVCs, our work suggests that group-13 thiospinels with $B^{III}_2X^{VI}_3$ and $A^{II}B^{III}_2X^{VI}_4$ (with a group-2 or group-12 *A* cation) compositions show a pressure behavior closer to tetrahedrally OVCs than to oxospinels or thiospinels with transition metals. In summary, this work paves the way to better understand the behaviour under pressure of compounds with $B^{III}_2X^{VI}_3$ and $A^{II}B^{III}_2X^{VI}_4$ composition. We hope this work will stimulate HP-XRD measurements on Al_2S_3 and spinel $ZnAl_2S_4$ that will be important to validate the hypothesis here stated and get a more complete picture of pressure-induced PTs in thiospinels.

Author Contributions

F. J. M. and O. G. conceived the project. S. G.-P., O. G. and F. J. M. planned and organized experiments. S. G.-P. analysed the data. Concerning the experimental part, HP-XRD measurements were carried out by R. V., V. P. C.-G, C. P. and F. J. M.; HP-Raman measurements by S. G.-P. Concerning the theoretical part, the total-energy and lattice dynamics DFT calculations were performed by P. R.-H. and A. M., meanwhile the minima hopping and evolutionary genetic methods for the structural search were performed by A. R., A.M. and R. A. The first manuscript draft was prepared by S. G.-P. The authors reviewed the manuscript and participated actively in the discussion of the results.

Conflicts of interest

There are no conflicts to declare.

Acknowledgments

The authors thank the financial support from Spanish Research Agency (AEI) under projects MALTA Consolider Team network (RED2018-102612-T) and projects PID2019-106383GB-41/42/43, as well as from Generalitat Valenciana under Project PROMETEO/2018/123 (EFIMAT) and the support from the US agencies under projects DMREF-NSF 1434897, and DOE DE-SC0016176. A. M., and P. R.-H acknowledge computing time provided by Red Española de Supercomputación (RES) and MALTA-Cluster, and we also thank ALBA synchrotron light source for funded experiment 2017022088 at the MSPD-BL04 beamline. A.H.R. acknowledges the computational resources awarded by XSEDE, a project supported by National Science Foundation grant number ACI-1053575, as well as the time from the Super Computing System (Thorny Flat) at WVU, which is funded in part by the National Science Foundation (NSF) Major Research Instrumentation Program (MRI) Award #1726534, and West Virginia University. The authors also acknowledge the support from the Texas Advances Computer Center (with the Stampede2 and Bridges supercomputers). A.M. and R.A acknowledge the support from Olle Engkvists stiftelse, Sweden, Carl Tryggers Stiftelse for Vetenskaplig Forskning (CTS) and the Swedish Research Council (Grant no. VR-2016-06014 and VR-2020-04410). SNIC and HPC2N are also acknowledged for providing computing resources.

Notes

* Corresponding authors: sagalpar@doctor.upv.es (S. G. -P.) and osgohi@fis.upv.es (O. G.).

References

1. N. Naghavi, S. Spiering, M. Powalla, B. Cavana and D. Lincot, *Progress in Photovoltaics: Research and Applications*, 2003, **11**, 437-443.
2. D. Hariskos, S. Spiering and M. Powalla, *Thin Solid Films*, 2005, **480**, 99-109.
3. N. Allsop, A. Schönmann, H. J. Muffler, M. Bär, M. C. Lux-Steiner and C. H. Fischer, *Progress in Photovoltaics: Research and Applications*, 2005, **13**, 607-616.
4. S. Rasool, K. Saritha, K. R. Reddy, M. Tivanov, A. Trofimova, S. Tikoto, L. Bychto, A. Patryn, M. Maliński and V. Gremenok, *Current Applied Physics*, 2019, **19**, 108-113.
5. N. Barreau, *Solar Energy*, 2009, **83**, 363-371.
6. S.-H. Choe, T.-H. Bang, N.-O. Kim, H.-G. Kim, C.-I. Lee, M.-S. Jin, S.-K. Oh and W.-T. Kim, *Semiconductor science and technology*, 2001, **16**, 98.
7. P. Rao and S. Kumar, *Thin Solid Films*, 2012, **524**, 93-99.
8. Y. X. Chen, A. Yamamoto and T. Takeuchi, *J. Alloys Compd.*, 2017, **695**, 1631-1636.
9. Y. X. Chen, K. Kitahara and T. Takeuchi, *J. Appl. Phys.*, 2015, **118**, 245103.
10. J. Zhang, H. Wang, X. Yuan, G. Zeng, W. Tu and S. Wang, *Journal of Photochemistry and Photobiology C: Photochemistry Reviews*, 2019, **38**, 1-26.
11. L. Wang, S. K. Karuturi and L. Zan, *Applied Surface Science*, 2020, 148063.
12. K. Hara, K. Sayama and H. Arakawa, *Solar Energy Materials and Solar Cells*, 2000, **62**, 441-447.
13. N. Barreau, C. Deudon, A. Lafond, S. Gall and J. Kessler, *Solar energy materials and solar cells*, 2006, **90**, 1840-1848.
14. X. Fu, X. Wang, Z. Chen, Z. Zhang, Z. Li, D. Y. Leung, L. Wu and X. Fu, *Applied Catalysis B: Environmental*, 2010, **95**, 393-399.
15. C.-H. Ho, M.-H. Lin, Y.-P. Wang and Y.-S. Huang, *Sensors and Actuators A: Physical*, 2016, **245**, 119-126.
16. W. Huang, L. Gan, H. Yang, N. Zhou, R. Wang, W. Wu, H. Li, Y. Ma, H. Zeng and T. Zhai, *Adv. Funct. Mater.*, 2017, **27**, 1702448.
17. H. Hahn and W. Klingler, *Zeitschrift für anorganische Chemie*, 1949, **260**, 97-109.
18. C. Adenis, J. Olivier-Fourcade, J.-C. Jumas and E. Philippot, *Revue de chimie minérale*, 1987, **24**, 10-21.

Please do not adjust margins

Please do not adjust margins

19. G. King, *Acta Crystallographica*, 1962, **15**, 512-512.
20. G. Steigmann, H. Sutherland and J. Goodyear, *Acta Crystallographica*, 1965, **19**, 967-971.
21. N. S. Rampersadh, A. M. Venter and D. G. Billing, *Phys. B*, 2004, **350**, E383-E385.
22. P. Donohue, *J. Solid State Chem.*, 1970, **2**, 6-8.
23. K.-J. Range and H.-J. Hübner, *Zeitschrift für Naturforschung B*, 1973, **28**, 353-355.
24. J. Van Landuyt, H. Hatwell and S. Amelinckx, *Mater. Res. Bull.*, 1968, **3**, 519-528.
25. R. Diehl and R. Nitsche, *Journal of Crystal Growth*, 1975, **28**, 306-310.
26. P. Pistor, J. M. Merino Álvarez, M. León, M. Di Michiel, S. Schorr, R. Klenk and S. Lehmann, *Acta Crystallographica Section B: Structural Science, Crystal Engineering and Materials*, 2016, **72**, 410-415.
27. H. Schäfer, G. Schäfer and A. Weiss, *Zeitschrift für anorganische und allgemeine Chemie*, 1963, **325**, 77-88.
28. P. Wyżga, W. Carrillo-Cabrera, L. Akselrud, I. Veremchuk, J. Wagler, C. Hennig, A. A. Tsirlin, A. Leithe-Jasper, E. Kroke and R. Gumeniuk, *Dalton Transactions*, 2020, **49**, 15903-15913.
29. A. Lafond, X. Rocquefelte, M. Paris, C. Guillot-Deudon and V. Jouenne, *Chemistry of Materials*, 2011, **23**, 5168-5176.
30. P. Wyżga, I. Veremchuk, C. Himcinschi, U. Burkhardt, W. Carrillo-Cabrera, M. Bobnar, C. Hennig, A. Leithe-Jasper, J. Kortus and R. Gumeniuk, *Dalton Transactions*, 2019, **48**, 8350-8360.
31. P. Wyżga, S. Grimm, V. Garbe, E. Zuñiga-Puelles, C. Himcinschi, I. Veremchuk, A. Leithe-Jasper and R. J. J. o. M. C. C. Gumeniuk, 2021, **9**, 4008-4019.
32. R. Diehl and R. Nitsche, *Journal of Crystal Growth*, 1973, **20**, 38-46.
33. R. Diehl, C. D. Carpentier and R. Nitsche, *Acta Crystallographica Section B*, 1976, **32**, 1257-1260.
34. A. Likforman and M. Guittard, *Comptes Rendus des Séances de l'Académie des Sciences–Paris, Série C*, 1974, **279**, 33.
35. K. J. Range and M. Zabel, *Zeitschrift für Naturforschung B*, 1978, **33**, 463-464.
36. J. Flahaut, Masson, 1952.
37. X. Lai, F. Zhu, Y. Wu, R. Huang, X. Wu, Q. Zhang, K. Yang and S. Qin, *J. Solid State Chem.*, 2014, **210**, 155-159.
38. B. Yao, H. Zhu, S. Wang, P. Wang and M. Zhang, *J. Solid State Chem.*, 2014, **210**, 150-154.
39. Y. Li, Q. Wang, Y. Gao, B. Liu, C. Gao and Y. Ma, *Materials Research Express*, 2017, **4**, 085902.
40. Y. Li, Y. Gao, N. Xiao, P. Ning, L. Yu, J. Zhang, P. Niu, Y. Ma and C. Gao, *AIP Advances*, 2018, **8**, 115202.
41. K. Liu, L. Dai, H. Li, H. Hu, L. Yang, C. Pu and M. Hong, *Chemical Physics*, 2019, **524**, 63-69.
42. F. Manjón, R. Vilaplana, O. Gomis, E. Pérez-González, D. Santamaría-Pérez, V. Marín-Borrás, A. Segura, J. González, P. Rodríguez-Hernández and A. Muñoz, *phys. status solidi (b)*, 2013, **250**, 669-676.
43. S. Klotz, J. C. Chervin, P. Munsch and G. Le Marchand, *J. Phys. D: Appl. Phys.*, 2009, **42**, 075413.
44. D. Errandonea, A. Muñoz and J. Gonzalez-Platas, *J. Appl. Phys.*, 2014, **115**, 216101.
45. F. Fauth, I. Peral, C. Popescu and M. Knapp, *Powder Diffraction*, 2013, **28**, S360-S370.
46. A. Dewaele, P. Loubeyre and M. Mezouar, *Phys. Rev. B*, 2004, **70**, 094112.
47. C. Prescher and V. B. Prakapenka, *High Pressure Research*, 2015, **35**, 223-230.
48. B. H. Toby and R. B. Von Dreele, *Journal of Applied Crystallography*, 2013, **46**, 544-549.
49. H. K. Mao, J. A. Xu and P. M. Bell, *Journal of Geophysical Research: Solid Earth*, 1986, **91**, 4673-4676.
50. A. Debernardi, C. Ulrich, M. Cardona and K. Syassen, *phys. status solidi (b)*, 2001, **223**, 213-223.
51. B. Garcia-Domene, H. Ortiz, O. Gomis, J. Sans, F. Manjón, A. Muñoz, P. Rodríguez-Hernández, S. Achary, D. Errandonea and D. Martínez-García, *J. Appl. Phys.*, 2012, **112**, 123511.
52. P. Hohenberg and W. Kohn, *Physical review*, 1964, **136**, B864.
53. G. Kresse and J. Hafner, *Phys. Rev. B*, 1993, **47**, 558.
54. P. E. Blöchl, *Phys. Rev. B*, 1994, **50**, 17953.
55. G. Kresse and D. Joubert, *Phys. Rev. B*, 1999, **59**, 1758.
56. J. P. Perdew, A. Ruzsinszky, G. I. Csonka, O. A. Vydrov, G. E. Scuseria, L. A. Constantin, X. Zhou and K. Burke, *Physical Review Letters*, 2008, **100**, 136406.
57. H. J. Monkhorst and J. D. Pack, *Phys. Rev. B*, 1976, **13**, 5188.

Please do not adjust margins

Please do not adjust margins

58. K. Parlinski, Computer Code Phonon, see: http://www.computingformaterials.com/index.html).
59. M. Amsler and S. Goedecker, *The Journal of chemical physics*, 2010, **133**, 224104.
60. S. Goedecker, *The Journal of chemical physics*, 2004, **120**, 9911-9917.
61. A. R. Oganov and C. W. Glass, *The Journal of chemical physics*, 2006, **124**, 244704.
62. A. R. Oganov, A. O. Lyakhov and M. Valle, *Accounts of chemical research*, 2011, **44**, 227-237.
63. A. R. Oganov, Y. Ma, A. O. Lyakhov, M. Valle and C. Gatti, *Reviews in Mineralogy and Geochemistry*, 2010, **71**, 271-298.
64. A. O. Lyakhov, A. R. Oganov, H. T. Stokes and Q. Zhu, *Computer Physics Communications*, 2013, **184**, 1172-1182.
65. P. V. Bushlanov, V. A. Blatov and A. R. Oganov, *Computer Physics Communications*, 2019, **236**, 1-7.
66. K. Okhotnikov, T. Charpentier and S. J. J. o. c. Cadars, 2016, **8**, 1-15.
67. S. Gallego-Parra, R. Vilaplana, O. Gomis, E. L. da Silva, A. Otero-de-la-Roza, P. Rodríguez-Hernández, A. Muñoz, J. González, J. Sans and V. Cuenca-Gotor, *Phys. Chem. Chem. Phys.*, 2021, **23**, 6841-6862.
68. M. Takumi, Y. Koshio and K. Nagata, *phys. status solidi (b)*, 1999, **211**, 123-129.
69. R. Vilaplana, S. G. Parra, A. Jorge-Montero, P. Rodríguez-Hernández, A. Munoz, D. Errandonea, A. Segura and F. J. Manjón, *Inorganic chemistry*, 2018, **57**, 8241-8252.
70. J. L. Da Silva, A. Walsh and H. Lee, *Phys. Rev. B*, 2008, **78**, 224111.
71. K.-J. Range, W. Becker and A. Weiss, *Zeitschrift für Naturforschung B*, 1968, **23**, 1009 - 1009.
72. D. Santamaría-Pérez, M. Amboage, F. Manjón, D. Errandonea, A. Muñoz, P. Rodríguez-Hernández, A. Mújica, S. Radescu, V. Ursaki and I. Tiginyanu, *The Journal of Physical Chemistry C*, 2012, **116**, 14078-14087.
73. L. Gerward, J. S. Olsen and U. Benedict, *Physica B+C*, 1986, **144**, 72-78.
74. R. Hoppe, W. Lidecke and F. C. Frorath, *Zeitschrift für anorganische und allgemeine Chemie*, 1961, **309**, 49-54.
75. K.-J. Range, M. Keubler and A. Weiss, *Zeitschrift für Naturforschung B*, 1969, **24**, 1060-1061.
76. W. Schanow and K.-J. Range, *Mater. Res. Bull.*, 1983, **18**, 39-44.
77. H. Beister, S. Ves, W. Hönle, K. Syassen and G. Kühn, *Phys. Rev. B*, 1991, **43**, 9635.
78. P. Brüesch and C. Schüler, *J. Phys. Chem. Solids*, 1971, **32**, 1025-1038.
79. G. C. Mather, C. Dussarrat, J. Etourneau and A. R. West, *Journal of Materials Chemistry*, 2000, **10**, 2219-2230.
80. H. Porthault, R. Baddour-Hadjean, F. Le Cras, C. Bourbon and S. Franger, *Vibrational Spectroscopy*, 2012, **62**, 152-158.
81. M. M. Rahman, W.-Y. Chen, L. Mu, Z. Xu, Z. Xiao, M. Li, X.-M. Bai and F. Lin, *Nature communications*, 2020, **11**, 1-13.
82. J. Dismukes and J. White, *Inorganic Chemistry*, 1964, **3**, 1220-1228.
83. M. Onoda and M. Saeki, *Chemistry Letters*, 1980, **9**, 665-666.
84. F. K. McTaggart and A. Wadsley, *Australian Journal of Chemistry*, 1958, **11**, 445-457.
85. K. Kambas, J. Spyridelis and M. Balkanski, *phys. status solidi (b)*, 1981, **105**, 291-296.
86. P. Pistor, R. Caballero, D. Hariskos, V. Izquierdo-Roca, R. Wächter, S. Schorr and R. Klenk, *Solar Energy Materials and Solar Cells*, 2009, **93**, 148-152.
87. E. Kärber, K. Otto, A. Katerski, A. Mere and M. Krunks, *Materials Science in Semiconductor Processing*, 2014, **25**, 137-142.
88. S. Gallego-Parra, O. Gomis, R. Vilaplana, H. M. Ortiz, E. Perez-Gonzalez, R. Luna, P. Rodríguez-Hernández, A. Muñoz, V. Ursaki and I. Tiginyanu, *J. Appl. Phys.*, 2019, **125**, 115901.
89. R. Vilaplana, M. Robledillo, O. Gomis, J. A. Sans, F. J. Manjón, E. Pérez-González, P. Rodríguez-Hernández, A. Muñoz, I. M. Tiginyanu and V. V. Ursaki, *J. Appl. Phys.*, 2013, **113**, 093512.
90. R. Vilaplana, O. Gomis, E. Pérez-González, H. M. Ortiz, F. J. Manjón, P. Rodríguez-Hernández, A. Munoz, P. Alonso-Gutiérrez, M. L. Sanjuán, V. V. Ursaki and I. M. Tiginyanu, *J. Appl. Phys.*, 2013, **113**, 233501.
91. O. Gomis, R. Vilaplana, F. J. Manjón, E. Pérez-González, J. López-Solano, P. Rodríguez-Hernández, A. Muñoz, D. Errandonea, J. Ruiz-Fuertes, A. Segura, D. Santamaria-Pérez, I. M. Tiginyanu and V. Ursaki, *J. Appl. Phys.*, 2012, **111**, 013518.
92. R. Vilaplana, O. Gomis, F. J. Manjón, H. M. Ortiz, E. Pérez-González, J. López-Solano, P.

Please do not adjust margins

Please do not adjust margins

Rodríguez-Hernández, A. Muñoz, D. Errandonea, V. V. Ursaki and I. M. Tiginyanu, *The Journal of Physical Chemistry C*, 2013, **117**, 15773-15781.

93. J. A. Sans, D. Santamaría-Pérez, C. Popescu, O. Gomis, F. J. Manjón, R. Vilaplana, A. Muñoz, P. Rodríguez-Hernández, V. V. Ursaki and I. M. Tiginyanu, *The Journal of Physical Chemistry C*, 2014, **118**, 15363-15374.
94. D. Santamaria-Perez, O. Gomis, A. L. Pereira, R. Vilaplana, C. Popescu, J. A. Sans, F. J. Manjón, P. Rodriguez-Hernandez, A. Muñoz and V. V. Ursaki, *The Journal of Physical Chemistry C*, 2014, **118**, 26987-26999.
95. P. Canepa, R. M. Hanson, P. Ugliengo and M. Alfredsson, *Journal of Applied Crystallography*, 2011, **44**, 225-229.
96. E. Kroumova, M. Aroyo, J. Perez-Mato, A. Kirov, C. Capillas, S. Ivantchev and H. Wondratschek, *Phase Transitions: A Multinational Journal*, 2003, **76**, 155-170.
97. H. Lutz, W. Becker, B. Müller and M. Jung, *J. Raman Spectrosc.*, 1989, **20**, 99-103.
98. V. Ursaki, F. Manjón, I. Tiginyanu and V. Tezlevan, *J. Phys.: Condens. Matter*, 2002, **14**, 6801.
99. B. Weinstein, *Phys. Rev. B*, 2021, **104**, 054105.
100. Y. Sim, J. Kim and M.-J. Seong, *J. Alloys Compd.*, 2016, **685**, 518-522.
101. H. Izadneshana and V. Gremenok, *Journal of Applied Spectroscopy*, 2014, **81**, 765-770.
102. V. F. Gremenok, K. Ramakrishna Reddy, M. S. Tivanov and A. Patryn, 2017.
103. R. Souissi, N. Bouguila, M. Bendahan, T. Fiorido, K. Aguir, M. Kraini, C. Vázquez-Vázquez and A. Labidi, *Sensors and Actuators B: Chemical*, 2020, **319**, 128280.
104. V. V. Ursaki and I. M. Tiginyanu, in *Pressure-induced phase transitions in AB_2X_4 chalcogenide compounds*, eds. F.J. Manjón, I. Tiginyanu and V. Ursaki, Springer, 2014, ch. 213-235.
105. S. Shao, W. Zhu, J. Lv, Y. Wang, Y. Chen and Y. Ma, *npj Computational Materials*, 2020, **6**, 1-6.
106. B. García-Domene, J. Sans, O. Gomis, F. Manjón, H. Ortiz, D. Errandonea, D. Santamaría-Pérez, D. Martínez-García, R. Vilaplana and A. Pereira, *The Journal of Physical Chemistry C*, 2014, **118**, 20545-20552.

Please do not adjust margins